Building and Environment 259 (2024) 111628

Contents lists available at ScienceDirect

Building and Environment

journal homepage: www.elsevier.com/locate/buildenv

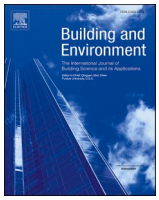

Wind-tunnel experiments on cross-ventilative cooling in a generic isolated building with one heated wall: Impact of opening size

Katarina Kosutova [a], Christina Vanderwel [b], Twan van Hooff [a,*], Bert Blocken [c,d], Jan L.M. Hensen [a]

[a] Building Physics and Services, Department of the Built Environment, Eindhoven University of Technology, P.O. box 513, 5600, MB Eindhoven, the Netherlands
[b] Aerodynamics and Flight Mechanics Research Group, University of Southampton, Boldrewood Innovation Campus, SO16 7QF, Southampton, United Kingdom
[c] Institute of Mechanical, Process and Energy Engineering, School of Engineering and Physical Sciences, Heriot-Watt University, Edinburgh, EH14 4AS, Scotland, United Kingdom
[d] Building Physics and Sustainable Design, Department of Civil Engineering, KU Leuven, Kasteelpark Arenberg 40 - bus 2447, 3001, Leuven, Belgium

ARTICLE INFO

Keywords:
Wind-tunnel experiments
Ventilative cooling
PIV
Indoor airflow
Heat flux
Indoor air temperature

ABSTRACT

This paper presents wind-tunnel experiments of cross-ventilative cooling in a generic isolated building with an interior heated side wall. Two different sizes of openings are considered: large and small openings. Particle image velocimetry (PIV) is used to determine velocities in the vertical centerplane. Air temperatures in the vertical centerplane are measured using negative temperature coefficient (NTC) sensors. Surface temperatures on the heated wall are measured using an infrared camera. Surface heat fluxes are obtained using heat flux sensors. In both cases the indoor airflow is dominated by the jet through the openings, with higher velocities in the building with large openings. The air temperatures measured with small openings are up to 7.5 % larger than those with large openings. The surface heat fluxes are up to 20 % higher in the building with large openings. The interior convective heat transfer coefficients vary considerably across the heated wall for both opening sizes and can be very different (up to 5 times higher) from those obtained by existing internal convective heat transfer coefficient correlations. The measurement results give insight into the complexity of ventilative cooling and can be used to validate computational fluid dynamics (CFD) simulations of cross-ventilative cooling.

1. Introduction

Natural ventilation is a commonly used technique to provide an energy-efficient and healthy indoor environment [1–8]. It can also be used as a passive cooling measure to decrease building cooling demands, using either day-time ventilative cooling, where heat gains are directly removed by outdoor air flowing through the building or night-time ventilative cooling. During night-time ventilative cooling, cold outdoor air flows through the building and cools down the indoor air volume and subsequently the thermal mass of the building, thus reducing the indoor air temperatures at the beginning of the next day and the cooling demand over this day. Various researchers explored the possibility of ventilative cooling to reduce the cooling load of buildings. Artmann et al. [9] investigated the potential of night-time ventilation and found that there is a significant to high potential for its use across Europe. Geros et al. [10] investigated the application of night ventilation techniques in ten urban canyons and concluded that it is essential to use appropriate meteorological data for the study and wind conditions representative of conditions within the urban canyon. Santamouris et al. [11] analyzed energy data from 214 air-conditioned residential buildings in which night-time ventilation techniques were applied. They concluded that night-time ventilation applied to residential buildings can reduce the cooling load with up to 40 kWh/m^2/y. The ability of night ventilation to reduce cooling loads of buildings was also confirmed by Wu et al. [12], who studied coupling night ventilation with active cooling for large supermarkets in China. These authors also concluded that night ventilation can reduce the peak cooling loads and reduce indoor temperatures. In addition to reducing the cooling loads of buildings, ventilative cooling may improve thermal comfort of the occupants. For example, da Graça et al. [13] investigated the performance of two passive cooling strategies (day-time ventilation and night-time cooling) in a six-story suburban building in Beijing and Shanghai. Based on the results, da Graça et al. [13] concluded that night cooling is superior to daytime ventilation in both cases and that night cooling has

* Corresponding author.
E-mail address: t.a.j.v.hooff@tue.nl (T. van Hooff).

https://doi.org/10.1016/j.buildenv.2024.111628
Received 17 September 2023; Received in revised form 21 April 2024; Accepted 9 May 2024
Available online 12 May 2024

the potential to significantly reduce the cooling load of buildings and improve the thermal comfort of the occupants. Ramponi et al. [14] investigated the effects of pressure coefficients (C_p) obtained from primary (e.g. wind tunnel experiments) or secondary (e.g. correlations from literature) sources on the energy saving potential of night ventilative cooling for six different European climates using an airflow network model. The authors concluded that the differences in calculated night ventilation rates were up to 15 % due to the different sources of C_p, however, they had only a small influence on total cooling effects. In addition, they reported that the choice of correct convective heat transfer coefficients (CHTC) is more crucial than the choice of C_p values in building energy simulations.

Furthermore, several studies focused on the sensitivity of night cooling performance on the internal CHTC (e.g. Refs. [15–18]). However, to the best knowledge of the authors, only Le Dreau et al. [16] experimentally derived internal CHTCs for mixing and displacement ventilation using a test room at Aalborg University [19]. Le Dreau et al. [16] subsequently compared the derived CHTCs with existing correlations and concluded that existing correlations provided relatively accurate results for displacement ventilation or for surfaces that are not directly affected by the inlet air (e.g. floors). Furthermore, large deviations were observed for forced convective heat transfer close to the inlet. The authors suggested that using the local air velocity as a parameter in these correlations could yield more favorable results.

In most cases, night ventilative cooling studies are (a) experimental (full-scale or reduced-scale measurements) ([3,10,17,18,20] [-][24]), (b) numerical, using either building energy simulation tools (e.g. ESP-r, EnergyPlus, TRNSYS) or computational fluid dynamics (CFD) (e.g. Refs. [3,13,15,16,23–26]), or (c) a combination of both (e.g. Refs. [20,21]). It is not always possible to construct a full-scale building model or to measure in existing buildings and the data resolution is very often low [3]. Wind-tunnel experiments can provide high-quality and high-resolution information about the indoor airflow and temperature distribution (in non-isothermal cases) in a reduced-scale building model. However, some difficulties may arise from the need for dynamic similarity. The Reynolds number (Re) has to be higher than at least the critical value of 10,000 in order to ensure that the flow is fully turbulent and independent of the Re number (e.g. Ref. [27]). When thermal effects are considered during the experiments, fulfilling similarity criteria becomes even more complicated or sometimes even impossible. The presence of buoyancy can in some cases significantly influence the flow field in or around the building; therefore, it is necessary to respect similarity criteria, expressed in terms of equal Prandtl (Pr) and Grashof (*Gr*) numbers in full scale and reduced scale, as much as possible. However, in case of studies with low air speeds and moderate temperature differences, the influence of Pr can be neglected (e.g. Ref. [28]). The *Gr* number on the other hand is important since it indicates whether the free convective flow close to the heated surface is turbulent or laminar. According to Ruck [28], and Bejan and Lage [29], $Gr > 10^9$ ensures free turbulent convection for a vertical heating plate. In addition, Ruck [28] stated that values of *Gr* just below the threshold of 10^9 do not affect the state of the flow. It is not always possible to achieve $Gr > 10^9$ in reduced-scale experiments due to limitations in the test-section size, and/or restrictions in the wind speed and temperature range. For example, Richards et al. [30] were only able to achieve $Gr \approx 10^8$ in their wind-tunnel experiments of wind flow around a building block subjected to thermal effects (wall heating).

Table 1 provides an overview of previous wind-tunnel studies on cross-ventilation in buildings. However, the majority of these studies were conducted under isothermal conditions. For example, Karava et al. [4] performed wind-tunnel experiments for a cross-ventilated single-zone building using particle image velocimetry (PIV) to measure outdoor and indoor velocities, and pressure taps to measure external and internal pressures. Tominaga and Blocken [31,32] used a similar building configuration to investigate cross-ventilation and contaminant dispersion in generic buildings in sheltered and unsheltered conditions. These authors provided a dataset of mean and rms velocities and mean and rms contaminant concentrations measured inside the building. The only non-isothermal study in Table 1 was performed by Carey and Etheridge [33]. They analyzed the feasibility of wind-tunnel experiments to obtain ventilation rates and they tested three different scenarios: wind-driven ventilation, buoyancy-driven ventilation and mixed ventilation (i.e. wind and buoyancy combined). Carey and Etheridge [33] concluded that the use of wind-tunnel experiments to estimate airflow rates can be a potentially powerful technique for buildings in order to specify the required size and position of the openings.

Table 1 shows that there is a lack of experimental data for non-isothermal cross-ventilation flows in buildings. Carey and Etheridge [33] presented their results in terms of discharge coefficients and dimensionless ventilation rates. Therefore, the present paper provides results of wind-tunnel experiments of cross-ventilation flow and cross-ventilative cooling for a generic isolated single-zone cubic building with an interior heated side wall. The experiments are performed for two different opening sizes: large (12.5 % facade porosity) and small (6.2 % facade porosity). Mean velocity, turbulent kinetic energy and air temperatures are measured in the vertical centerplane and surface temperature and surface heat fluxes are measured on the interior heated wall. The aim of this study is twofold: (1) to analyze the indoor environment in terms of mean velocity, turbulent kinetic energy, air temperature, surface temperature and surface heat fluxes in case of

Table 1
Non-exhaustive overview of wind-tunnel experiments on cross-ventilation.

Authors	Ref.	Wind tunnel	Exp. model	Measured	Method	Iso/Non-iso
Murakami (1991)	[34]	Not specified	Cross-ventilated cube	V, P, C	TA, HWA, CM, TGM	Isothermal
Katayama et al. (1992)	[35]	Open-circuit WT	Urban area	V, P	HWA, DMM	Isothermal
Kato et al. (1992)	[36]	Not specified	Cross-ventilated cube	V, C,P	TGM, CM, TA, HWA	Isothermal
Carey & Etheridge (1999)	[33]	Low speed WT	Cross-ventilated RP	T, P	TC, TGM	Iso/Non-iso
Ohba et al. (2001)	[37]	Open-circuit WT	Cross-ventilated RP	V,C, P	SPF, PHA, MDPG	Isothermal
Jiang et al. (2003)	[38]	ABL WT	Cross-ventilated cube	V	LDA	Isothermal
Karava et al. (2007)	[39]	ABL WT	Cross-ventilated gable roof bld	Int. and ext. P	PT	Isothermal
Karava et al. (2011)	[4]	ABL WT	Cross-ventilated RP	V, ext. P, int. P	PIV, PT	Isothermal
Ji et al. (2011)	[40]	ABL WT	Cross-ventilated RP	C, DFR, P	FID	Isothermal
Lo et al. (2011)	[41]	ABL WT	Test house	Facade P	PT	Isothermal
Tecle et al. (2013)	[42]	ABL WT	Test house	Int. and ext. P	PT	Isothermal
Tominaga & Blocken (2015)	[31]	ABL WT	Cross-ventilated RP	V, C, TF	SFP, CTA, TGM, HSHA	Isothermal
Tominaga & Blocken (2016)	[32]	ABL WT	Cross-ventilated RP	V, C, TF	SFP, CTA, TGM, HSHA	Isothermal

Notes: WT – wind tunnel, Iso – isothermal, Non-iso – non-isothermal, ABL – atmospheric boundary layer, RP – rectangular parallelepiped, V – velocity, P – pressure, C – concentration, DFR – diluting flow rate, TF – turbulent fluxes, HWA – hot-wire anemometry, DMM – displacement micro manometers, TGM – tracer gas method, CM – capacitance manometer, TA – thermal anemometry, TC – thermocouples, SPF – split fiber probe, PHA – pressure hydrocarbon analyzer, MDPG – micro differential pressure gauge, LDA – laser Doppler anemometry, bld - building, PIV – particle image velocimetry, FID - flame ionization detector, PT – pressure taps, SFP – split fiber probe, HSHA – high speed hydrocarbon analyzer, CTA – constant thermal anemometry.

cross-ventilative cooling; (2) to compare internal CHTC values based on the measured temperature and heat fluxes with those available in the literature. To the best knowledge of the authors, a cross-ventilation study where mean velocities, air and surface temperatures and heat fluxes are measured during wind tunnel experiments has not yet been published.

The experimental setup is outlined in Section 2. The results from the measurements are presented in Section 3, after which a comparison of experimentally derived CHTCs with CHTC values based on both internal and external CHTC correlations from the literature is discussed in Section 4. Section 5 contains the limitations of the study and directions for future work, and Section 6 summarizes the main findings of the study.

2. Experimental setup

2.1. Wind-tunnel setup

The experiments are performed in an open-circuit wind tunnel at the University of Southampton, UK (e.g. Refs. [43,44]). The dimensions of the wind-tunnel test section are 0.9 × 0.6 × 4.5 m^3 (W × H × L). The incident flow is representative of the bottom part of a neutral atmospheric boundary layer (ABL) and is created using 427 mm high spires, three different types of roughness elements with decreasing heights (32, 16 and 7 mm high) and a carpet. The incident flow refers to the flow conditions in the empty wind tunnel at the location where the building would be positioned [45]. The roughness setup for these experiments is based on the work of Taddei et al. [43]. Fig. 1a shows the wind-tunnel setup including the PIV optics. The roughness setup in the wind tunnel is displayed in Fig. 1b. Fig. 1c shows the PIV setup in more detail.

The incident profiles of the mean streamwise velocity and turbulence intensity obtained by the PIV measurements are shown in Fig. 2a and b, respectively. The vertical profile of the mean streamwise velocity adheres to the logarithmic law:

$$U = \frac{u^{*}ABL}{k}\, ln\frac{y}{y_0} \tag{1}$$

where κ is the von Karman constant (0.42), u^*_{ABL} (m/s) is the ABL friction velocity and y_0 (m) is the aerodynamics roughness length. The values of $u^*_{ABL} = 0.195$ m/s and $y_0 = 0.0024$ m (reduced scale, 1:20) are calculated from a fit of the measured data. The roughness Reynolds number, defined as $Re^* = u^*_{ABL} \bullet y_0/\nu$, with $\nu = 1.56 \times 10^{-5}$ m^2/s the kinematic viscosity of air at 25.5 °C, is equal to 31.2, which satisfies the condition for a fully rough surface [27] for the given experimental conditions ($Re^* > 1$, as indicated in Ref. [27]). The turbulence intensities in the streamwise (I_u) and vertical (I_v) direction are calculated using Equation (2):

$$I_u = \frac{\sigma_u}{U_{ref}}, I_v = \frac{\sigma_v}{U_{ref}} \tag{2}$$

where U_{ref} (=1.9 m/s) is the incident mean velocity at the building

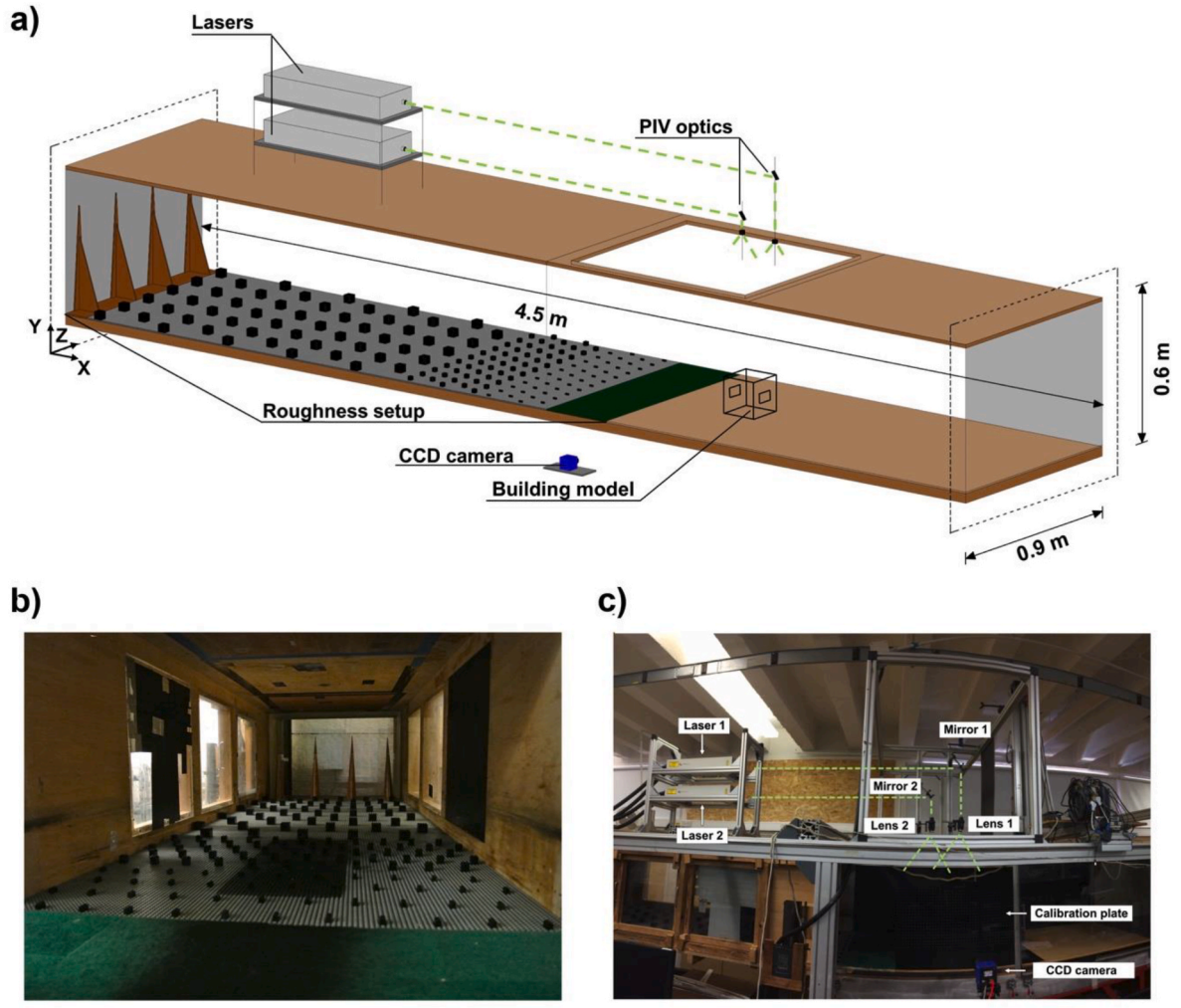

Fig. 1. (a) Experimental setup of the atmospheric boundary layer wind tunnel including equipment for the PIV measurements. (b) Roughness setup. (c) Detailed picture of the PIV setup.

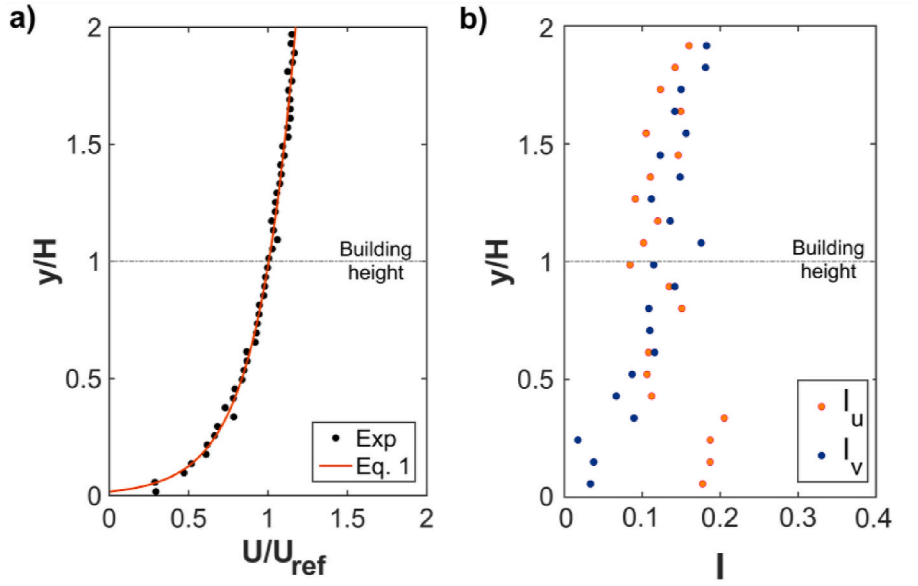

Fig. 2. Vertical incident profiles of: (a) Time-averaged streamwise velocity U/U_{ref}. (b) Turbulence intensity in streamwise (I_u) and vertical (I_v) direction.

height H (=0.15 m) and σ_u and σ_v are the standard deviations of the turbulent fluctuations in the streamwise and vertical direction, respectively. The streamwise turbulence intensity at the building height is about 10 % (Fig. 2b). This value is in the expected range for a y_0 value of 0.0024 m, which is about 0.05 m in full scale, i.e. a turbulence intensity of 5–20 % is expected for $y_0 \sim 0.05$ m according to the VDI 3783 guidelines (or the ESDU 85020). Although measurements of the integral length scale are not available, a separate measurement of the spectra at

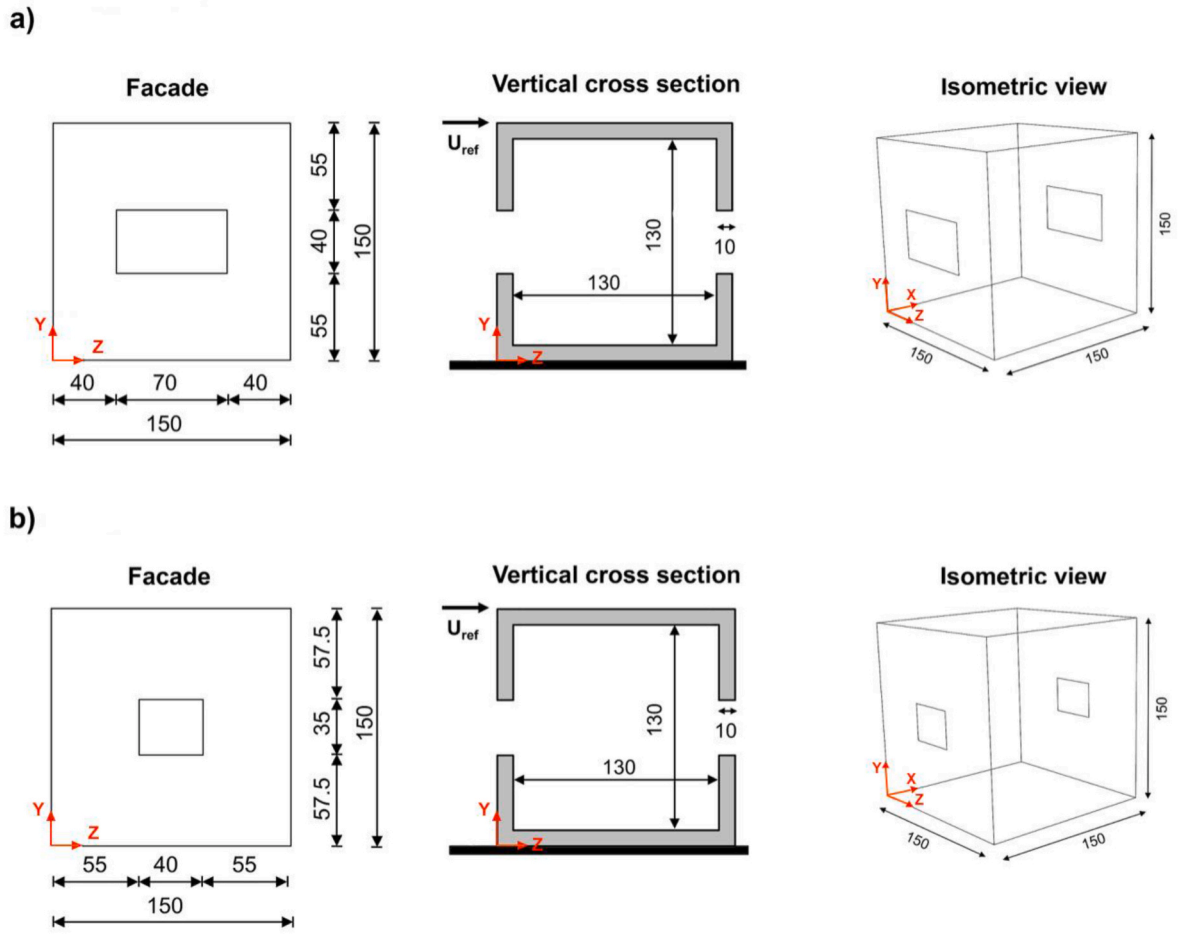

Fig. 3. Geometry of the building models used in the wind-tunnel experiments. (a) Building model with large openings (12 % facade porosity). (b) Building model with small openings (6 % facade porosity). All dimensions are in mm.

approximately the building height as reported by Taddei et al. [43], indicates that the inertial range of the flow spans scales from 10^{-2} to 10^{0} m, which reflects the wind tunnel dimensions and roughness geometry and suggests that the integral scale of the experiments is on the order of 1 m. ESDU data (as reported by Ref. [46]) suggests that the full-scale flow with $y_0 \sim 0.05$ m should exhibit integral scales on the order of 10^{1} m at the building height. Considering the scaling parameter of 1:20 this is in line with the measured value by Taddei et al. [43]. The exterior approach-flow temperature during the measurements is 25.5 °C. The building Reynolds number calculated using Equation (3) is about 18, 269.

$$Re = \left(U_{ref} \cdot H\right) / \nu \tag{3}$$

Where U_{ref} (=1.9 m/s) is the incident mean velocity at the building height H (=0.15 m) and ν (=15.56 × 10^{-6} m^2/s) is the kinematic viscosity of air at 25.5 °C.

The wind-tunnel experiments are carried out for the wind direction perpendicular to the facade with the openings.

2.2. Building model

The building model used for the wind-tunnel experiments (1:20 scale) is a single-zone cubic building with one opening in the windward and one opening in the leeward facade. The scale of 1:20 reflects the ratio of the model size to a typical single-story building. The building dimensions are 0.15 × 0.15 × 0.15 m^3 (Fig. 3). The building is made of 0.01 m thick polymethyl methacrylate (PMMA) sheets connected together by plastic bolts allowing testing with different window configurations. The wind-tunnel experiments are performed for two different sizes of the openings: (a) large openings (LO case) with window opening dimensions of 0.07 × 0.04 m^2 (W_O × H_O) yielding 12.5 % facade porosity (Fig. 3a) and (b) small openings (SO case) with window opening dimensions of 0.04 × 0.035 m^2 (W_O × H_O) yielding 6.2 % facade porosity (Fig. 3b). One side of the building wall (right-hand side when looking in the downstream direction) is equipped with a 0.75 mm thick clear polypropylene sheet (ViPrint Clear, Stephen Webster Plastics, UK) in order to provide a transparent surface for the thermal camera measurements of the opposite (heated) interior wall (Fig. 4a). This opposite wall is equipped with a heating plate to provide higher wall temperatures. The heating plate consists of a 1 mm thick brass plate with a surface temperature of 60 °C controlled by a temperature controller and is enclosed by two 3 mm thick sheets of extruded polystyrene. An aluminum plate of 2 mm is attached to the polystyrene sheet from the interior and it is covered by a 2 mm thick black polyvinyl chloride (PVC) plate – a detailed schematic of the heated wall is shown in Fig. 4b. In order to reduce reflections of the material during the PIV measurements, the edges of the building model, including the heads of the plastic bolts, are painted black.

The effect of buoyancy on the indoor airflow can be assessed using the Richardson number (Ri), which is the ratio of the Grashof number (*Gr*) to the square of building Reynolds number (Re) (Equation (4)) and is defined as:

$$Ri = \frac{Gr}{Re^2} = \frac{\beta g H\left(T_w - T_{ref}\right)}{U_{ref}^2} \tag{4}$$

where β = 0.00335 1/K is the thermal expansion coefficient of air at 25.5 °C, g = 9.81 m/s^2 is the gravitational acceleration, H = 0.15 m is the height of the building, T_w = 44 °C is the surface-averaged interior heated wall surface temperature measured when the wind tunnel was running in stationary wind speed and temperature conditions, T_{ref} = 25.5 °C is the time-averaged approach-flow reference air temperature (temperature of the ambient air in the wind tunnel) and U_{ref} = 1.9 m/s is the reference velocity, yielding Ri = 0.03. This Ri number is small, indicating that the indoor airflow is mainly induced by inertial forces, i.e. forced convection dominates over natural convection. It is not possible to achieve higher Ri numbers for several reasons. First, the size of the building model is restricted by the blockage ratio in the wind tunnel (Φ), which has to be kept under 5 % (e.g. Refs. [30,47]) (Φ = 4.2 % for current study). Second, in order to achieve a higher Ri number, the velocity of the approach flow could be lowered, however, this is again restricted by the wind tunnel setup due to a decreased flow stability for lower velocities than the one used in this study and because the building Reynolds number would drop below the minimum required value of 11, 000 [48]; therefore, it is not possible to perform proper experiments for velocities lower than 1.9 m/s. In subsection 4, dynamic similarity will be further discussed.

2.3. Velocity measurements

2D PIV measurements are carried out in the vertical centerplane parallel to the flow direction (Fig. 1) in accordance with the guidelines for PIV by Prasad [49]. The building is carefully aligned with the centerline of the wind tunnel ahead of testing to ensure that any outdoor and indoor flow asymmetry would be a result of the non-isothermal conditions imposed. Two double pulse 200–15 PIV Nd:YAG lasers are used to provide a laser sheet, illuminating the building model using a set of mirrors and cylindrical lenses. The flow entering the wind tunnel is seeded by means of a cold-smoke fog machine creating aerosol particles (average diameter is 1–1.5 μm) from a solution of demineralized water and glycol acting as passive flow tracers with negligible thermal effects.

Particle images are captured by a charged coupled device camera

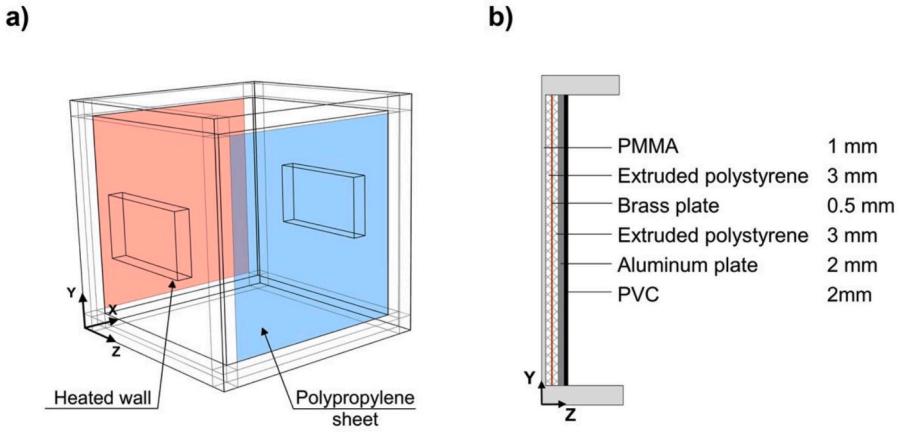

Fig. 4. (a) Isometric view of the building model indicating the position of the heated wall and polypropylene sheet. (b) Vertical cross-section of the heated wall with wall composition.

(CCD) (VC-Imager Pro Lx 16 M) equipped with an AF Nikkor 50 mm f/1.8D lens positioned normal to the laser sheet. For each window configuration, a set of 500 uncorrelated images is taken at a rate of 0.7 Hz resulting in a total measuring time of about 720 s. The PIV results are processed in DaVis 8.2.0 software from LaVision using an interrogation window size of 32 × 32 pixels and 50 % overlap. The uncertainty of the measurement results is around 1–5.5 % for both cases, however, in low velocity regions, the uncertainty can increase up to 10 %. The random uncertainty of the mean velocity is calculated as follows (e.g. Refs. [50, 51]):

$$u_r = \frac{1}{\sqrt{N}} \frac{Z_\alpha}{2} \frac{|V|RMS}{|V|} \quad (5)$$

where N is the number of frames, $z_\alpha/2$ corresponds to a variable related to the chosen confidence interval ($z_\alpha/2 = 1.96$ for 95 % confidence interval in this case), $|v|_{RMS}$ is the root mean square of the measured two-dimensional velocity magnitude in a point and $|V|$ corresponds to the mean two-dimensional velocity magnitude at the location of $|v|_{RMS}$. The PIV measurements are conducted for a mean incident velocity (U_{ref}) at roof height (H) of 1.9 m/s. Two sets of measurements are carried out, one for the building with large openings (LO case) and one for the building with small openings (SO case).

2.4. Temperature measurements

Surface temperatures at the heated wall are measured under stationary conditions using a mid-range infrared camera (FLIR SC7000) with temperature measurement accuracy ±1 % positioned normal to the heated wall. To enable surface temperature measurements, part of the wind-tunnel sidewall is made of a material that is transparent to the spectral range of the thermal camera. Therefore, the same polypropylene sheet as used in the experimental building model is used to construct the wind-tunnel side window for the infrared camera measurements (Fig. 5a). Indoor air temperatures are measured using NTC U-type sensors with a diameter of 2.4 mm and precision of 0.05 °C. They are measured at nine locations at each of the three measuring heights in the vertical centerplane (Fig. 5b). Only two sensors are used to simultaneously measure the air temperature at two locations while at the same time the remaining seven openings are aerodynamically sealed. The air temperatures are measured for 120 s to obtain stationary results.

2.5. Heat flux measurements

Surface heat fluxes on the heated wall are measured using six gSKIN-Xp 26 9C heat flux sensors (greenTeg) with dimensions 10 × 10 mm^2 and a precision of ±3 %. The location of the heat flux sensors on the heated wall is depicted in Fig. 5c. The sensors are mounted on the

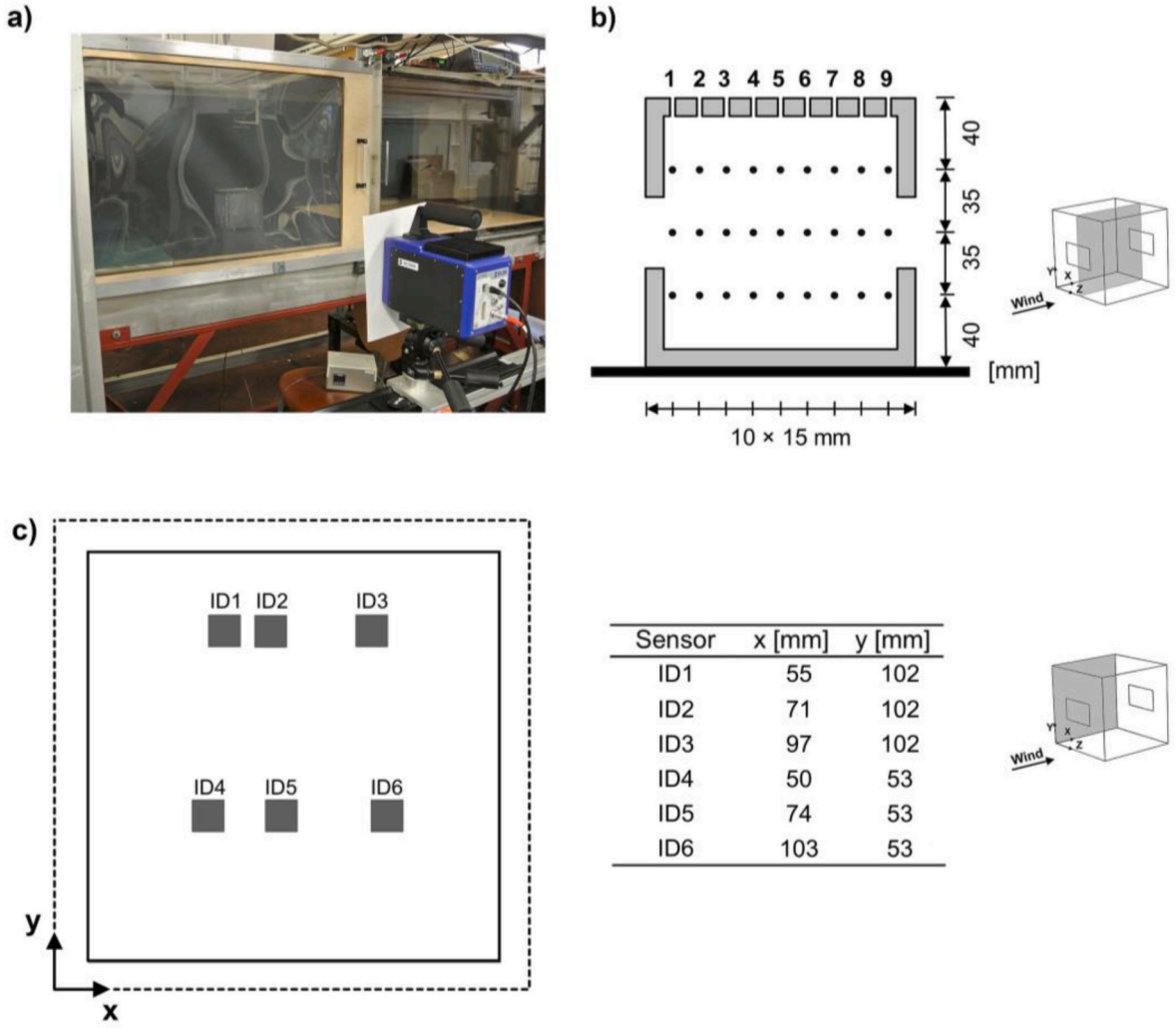

Sensor	x [mm]	y [mm]
ID1	55	102
ID2	71	102
ID3	97	102
ID4	50	53
ID5	74	53
ID6	103	53

Fig. 5. (a) Setup for the thermal camera measurements. (b) Positions for indoor air temperature measurements in a vertical centerplane. (c) Positions of the heat flux measurement sensors at indoor surface of heated wall. Note that the positions in x-direction were measured from the side edge while positions in y-direction were measured from the bottom edge of the heated wall to the center of the sensor. The dashed line represents the outer dimensions of the wall. All dimensions are in mm.

surface using thermal conductive paste. Time-averaging of the measured heat flux is conducted for a period of 120 s to obtain stationary values. The heat flux sensors are arranged on two lines – one at 53 mm above the floor and the other 102 mm above the floor (Fig. 5c). Note that the height at which measurement sensors are positioned is measured from the bottom edge of the heated wall to the center of the sensor. The sensors are connected to the data logger via cables passing through the floor of the wind tunnel. Note that due to the cables of the heat flux sensors it is not possible to place heat flux sensors directly above each other as the vertically oriented cables would pass through the sensors.

3. Results

3.1. Time-averaged velocity vector fields and contour plots

Time-averaged velocity vector fields in the vertical centerplane of the buildings with large and small openings are shown in Fig. 6a–b. For both cases, the flow through the building is dominated by a jet, which flows from one opening to the other, as was observed in earlier experimental isothermal cross-ventilation studies, for example [4,31,33]. However, the results from the present study show a smaller deflection of the jet. The jet accelerates right after passing through the windward opening (*vena contracta*) and the incoming jet is directed downwards, which can be attributed to the standing vortex in front of the building and to the pressure field near the windward building facade, with higher pressure above than below the opening. However, the jet does not reach the floor of the building. A stronger jet is visible in Fig. 6a for the LO case than in Fig. 6b for the SO case, which is due to the opening size.

Fig. 6c–d shows the contours of dimensionless time-averaged streamwise velocity (U/U_{ref}) for both cases. Note that the blue zones in the direct vicinity of the walls can be attributed to the applied mask in the PIV post-processing and are therefore not an indication of velocity magnitude. Fig. 6c shows that the jet in the LO case is wider and less deflected towards the floor compared to the jet in the SO case. Nevertheless, in both cases, the velocity noticeably decreases further downstream (around $x/H = 0.6$ for SO and around $x/H = 0.4$ for LO) with some recovery occurring close to the leeward opening. The jet half-widths ($\delta_{0.5}$) on both sides of the jet centerline are indicated with black dots in Fig. 6c and d. The jet half-width is calculated as the linear vertical distance between the local maximum jet velocity (i.e. the velocity at the jet centerline) and the location where the velocity is equal to half of this local maximum jet velocity (e.g. Ref. [52]). Note that the upper jet half-width is not always equal to the lower jet half-width due to the observed asymmetry of the jet. The jet spreading parameter is then calculated as follows: $(\delta_{0.5,upper} + \delta_{0.5,lower})/H_o$ with H_o the height of the opening ($H_o = 0.04$ m for LO case and $H_o = 0.035$ m for SO case). The maximum jet spreading in the area where the jet is directed downward ($0.1 \leq x/H \leq 0.7$) for the LO case is 1.12 and occurs at $x/H = 0.7$, while for the SO case it is 1.18 and occurs at $x/H = 0.7$. The maximum jet spreading is thus 12 % and 18 % larger than the height of the opening through which the jet enters the building, for the LO and SO case, respectively.

Fig. 6e shows the measured jet trajectory based on the local maximum jet streamwise velocity (U_{max}) for both cases. The points represent the location of U_{max} along nine vertical lines in the vertical centerplane of the building model. The results from the SO case show a slightly stronger deflection of the jet towards the floor. The incoming jet angle is calculated for both cases based on the vertical location of U_{max} at the windward opening ($x/H = 0$) and at $x/H = 0.6$ (the jet in both cases still shows a downward direction at this location) (Fig. 6f) using Eq. (6).

$$\alpha = tan^{-1}\left(\frac{y_{max;x/H=0} - y_{max;x/H=0.6}}{0.6H}\right) \quad (6)$$

The incoming jet angle for the LO case is $\alpha_{LO} = 11^\circ$ while for the SO case it is $\alpha_{SO} = 15^\circ$, again illustrating the larger deflection of the incoming jet to the ground in the SO case. This difference can possibly be attributed to a slightly different pressure distribution on the windward facade for both cases caused by a different size of the standing vortex in front of the building, as Kurabuchi et al. [53] indicated this as main reason for the downward jet flow in cross-ventilation cases.

Fig. 7 shows dimensionless time-averaged streamwise velocities (U/U_{ref}) along nine vertical lines spaced 15 mm apart. Fig. 7a–c indicates that the differences in vertical profiles between LO and SO cases increase as the location gets further from the windward opening. The maximum velocities along the first two lines are located at approximately the same height for both openings ($y/H \approx 0.52$–0.53). Close to the central part of the building (Fig. 7d–f), the maximum value of U/U_{ref} for the LO case is up to 25 % larger than for the SO case. Close to the leeward wall (Fig. 7g–i), the velocities are still higher for the LO case, however, the upward deflection of the jet is only slightly different from the SO case due to the influence of the leeward wall (Fig. 7i). The maximum velocity for the LO case ($U_{max;LO}/U_{ref} = 0.68$)) is reached at the location $x/H = 0.2$, $y/H = 0.5$. For the SO case, the maximum velocity ($U_{max;SO}/U_{ref} = 0.65$) is reached at the location $x/H = 0.2$, $y/H = 0.45$. The difference between the maximum velocities is 5 %, however, as shown in Fig. 7d–g, the velocity decrease in downstream direction in the central part of the building is larger in the SO case.

Since the flow pattern has clear vertical components (see Fig. 6a and b), the dimensionless time-averaged vertical velocities (V/U_{ref}) along nine vertical lines are presented in Fig. 8a–i. Velocities obtained for the LO and SO cases are very similar with only relatively minor differences, which are mainly present in the direct vicinity of the openings (i.e. $x/H = 0.1$ and $x/H = 0.9$). For example, the vertical velocity at $x/H = 0.9$ and $y/H = 0.8$ is almost zero for the LO case, while it is almost -0.1 for the SO case.

Values of U/U_{ref} along the horizontal centerline ($y/H = 0.5$) are shown in Fig. 9 for both cases An acceleration due to the vena contracta is followed by a strong deceleration of the flow, after which some recovery of the velocity takes place near the leeward opening. Values of U/U_{ref} for the LO case are up to 103 % larger (at $x/H = 0.63$) compared to the SO case, although the mean velocities at $x/H = 0.1$ are similar ($U/U_{ref} = 0.63$), indicating the much larger mean velocity gradient in streamwise direction for the SO case.

Fig. 10 shows the dimensionless time-averaged turbulent kinetic energy (k/U_{ref}^2) along five vertical lines. Note that the results of turbulent kinetic energy along lines $x/H = 0.1$, 0.2, 0.8 and 0.9 are not included, since they were considered to be unreliable (showing unphysical values in these regions). Peaks in turbulent kinetic energy are present at two locations and originate from the upper and lower edges of the window openings ($y/H = 0.4$ and $y/H = 0.6$) and from the shear layers bounding the jet. These peaks are most pronounced between $0.3 \leq x/H \leq 0.5$ for LO and $0.3 \leq x/H \leq 0.4$ for SO. Turbulent kinetic energy measured at the upper peak for LO is up to 25 % higher at $x/H = 0.3$ and 1.4 % at $x/H = 0.4$ than the one measured at the upper peak for SO case. However, turbulent kinetic energy measured at the lower peak is up to 51 % larger for SO at $x/H = 0.4$. A clear reason for the former cannot be found using the measurement data available. The latter observation corresponds to what one would expect based on the smaller opening area resulting in higher contraction of the flow and therefore increased turbulence levels for the SO case. It must be noted that there is only a limited decrease in opening height for SO compared to LO (35 mm vs. 40 mm), which could play a role in the absence of a clear trend with respect to turbulence levels measured along the five presented vertical lines in the vertical center plane. The magnitude of these peaks of turbulent kinetic energy is decreasing towards the leeward opening due to the dissipation and reduced production of turbulence because of the reducing shear layer strength.

3.2. Temperatures

The dimensionless time-averaged indoor air temperatures measured

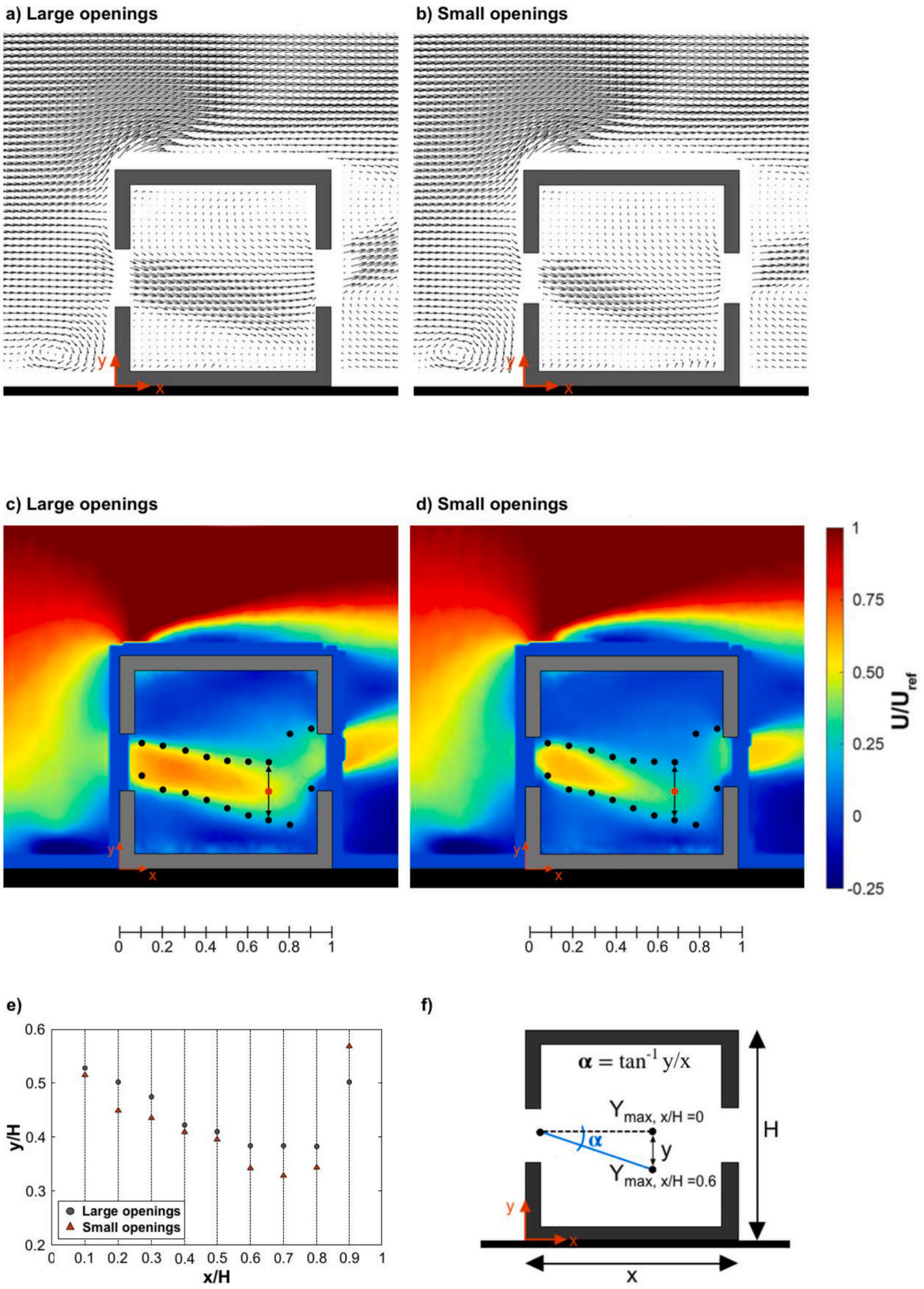

Fig. 6. PIV results for the case with large openings (a,c) and small openings (b,d) in the vertical centerplane (z/H = 0.5)
(a, b) Time-averaged velocity vector fields. (c,d) Dimensionless time-averaged streamwise velocity contours with indication of jet half-widths ($\delta_{0.5,\ upper}$ and $\delta_{0.5,\ lower}$).(e) Vertical location of time-averaged maximum streamwise velocity (U_{max}) along nine vertical lines. (f) Definition of incoming jet angle (α) based on the vertical location of maximum streamwise velocity U_{max}.

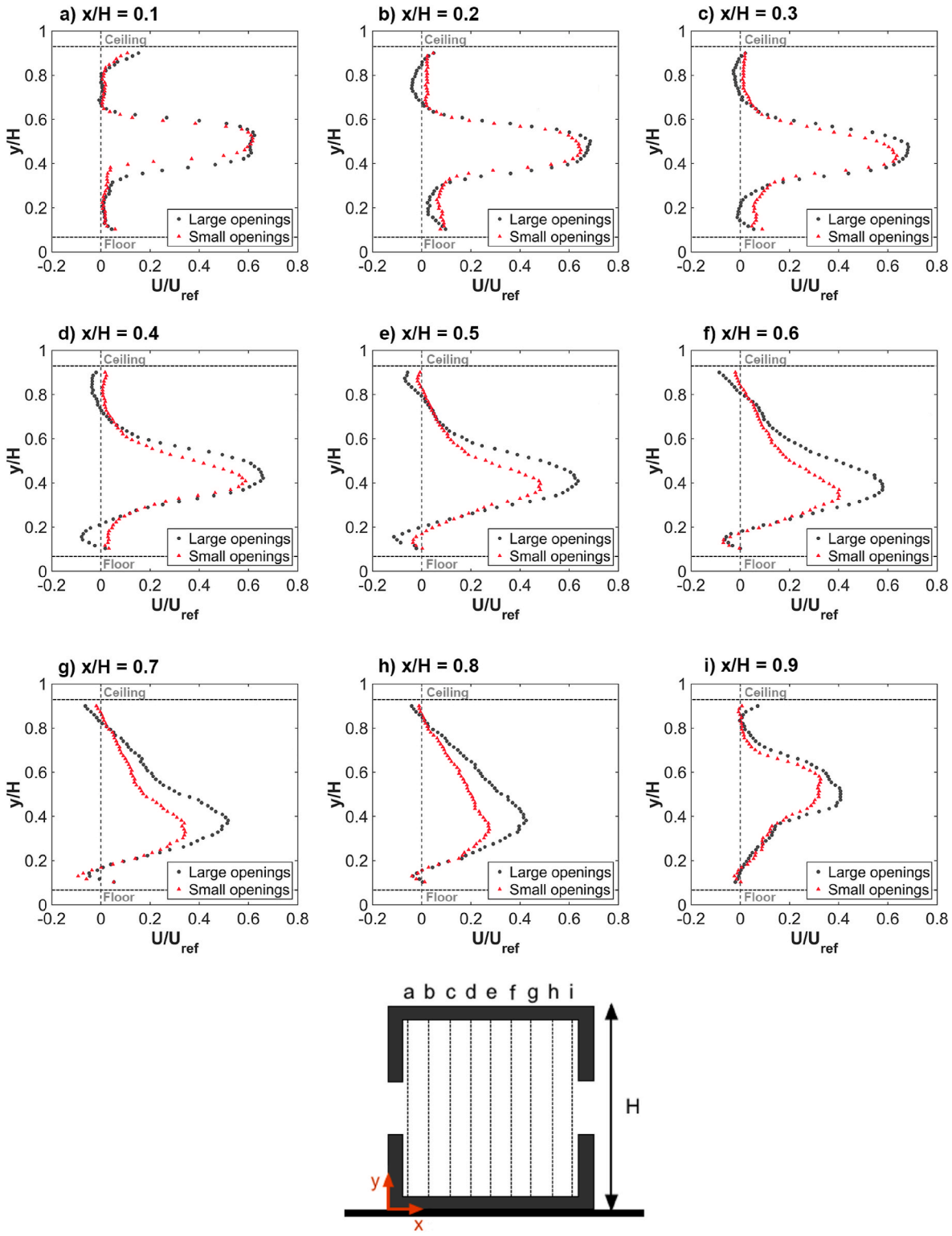

Fig. 7. Dimensionless time-averaged vertical profiles of streamwise velocity component, U/U_{ref}, for large and small openings along nine lines in the vertical centerplane (z/H = 0.5); H = 0.15 m, U_{ref} = 1.9 m/s.

along three horizontal lines are depicted in Fig. 11a–c. Note that the air temperatures are normalized using the reference temperature: T_{ref} = 25.5 °C for both openings. The time-averaged air temperatures measured along the bottom horizontal line (y/H = 0.25; Fig. 11a) in the vertical centerplane are closest to the inlet air temperatures; the average values of these dimensionless time-averaged temperatures, $(T-T_{ref})/T_{ref}$, along this line are 0.03 (3 % higher than T_{ref}) for the LO case and 0.07 (7 % higher than T_{ref}) for the SO case.

The minimum dimensionless time-averaged air temperature along the horizontal centerline (Fig. 11b) is 0 (25.5 °C) for the LO case and 0.04 for the SO case, and these are measured in the middle of the jet close to the windward opening (at x/H = 0.1 and x/H = 0.2). From x/H = 0.2, the temperatures are gradually increasing towards the leeward opening in both cases, due to the fresh air from the windward opening

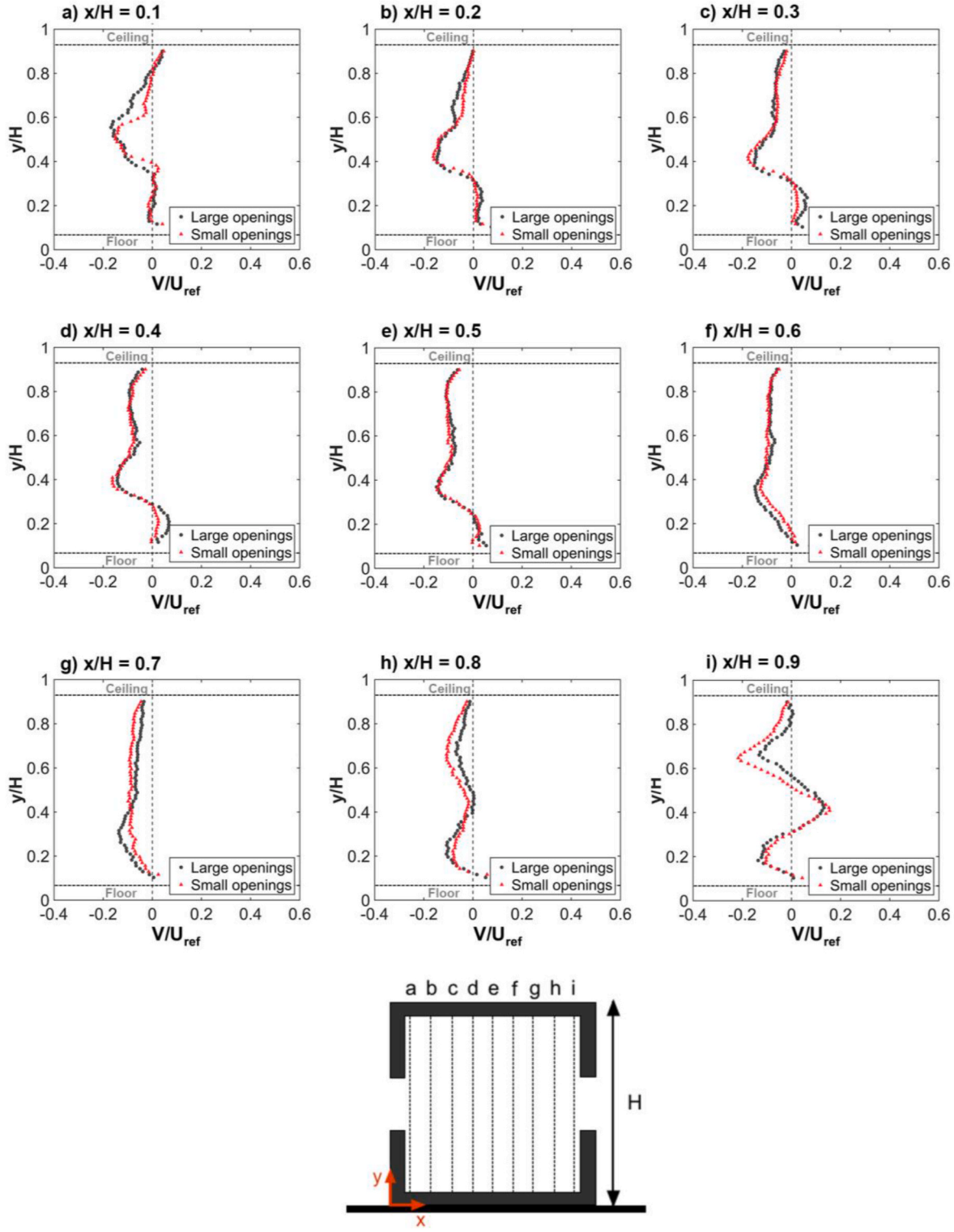

Fig. 8. Dimensionless time-averaged vertical profiles of vertical velocity component, V/U_{ref}, for large and small openings along nine lines in the vertical centerplane ($z/H = 0.5$); $H = 0.15$ m, $U_{ref} = 1.9$ m/s.

transporting the heated room air towards the leeward opening. For the LO case, the air temperatures are decreasing closer to the leeward opening ($x/H > 0.7$).

The highest time-averaged air temperature is measured along the line in the upper part of the building model (Fig. 11c). Temperatures measured along this line are on average 15 % (LO case) and 21 % (SO case) higher than the reference temperature. In both cases, the velocities in this part of the building interior are low (see Fig. 7), thus the air temperatures along the upper horizontal line increase due to the heat generation from the heated wall, which is convected towards the middle of the enclosure, but remains in the upper part due to the specific flow pattern with the downward directed incoming jet. The highest dimensionless time-averaged temperature is measured along the upper horizontal line ($y/H = 0.75$, Fig. 11c), i.e. $(T\text{-}T_{ref})/T_{ref} = 0.2$ for the LO case

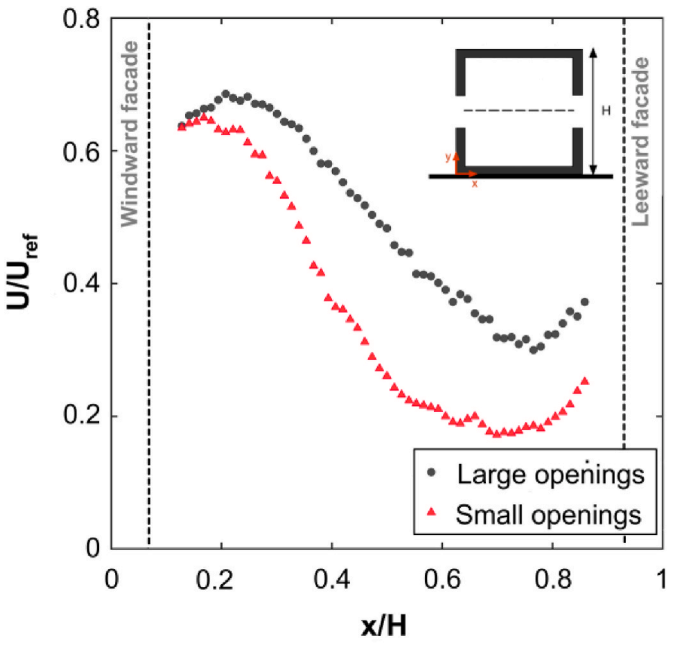

Fig. 9. Dimensionless time-averaged profiles of streamwise velocity component, U/U_{ref} for large and small openings along the horizontal centerline (y/H = 0.5, z/H = 0.5), U_{ref} = 1.9 m/s.

at x/H = 0.6 and $(T-T_{ref})/T_{ref}$ = 0.23 for the SO case at x/H = 0.8, i.e. 20 % and 23 % higher than the reference temperature, respectively. Overall, the air temperatures measured for the SO case are up to 7.5 % higher than the air temperatures measured for the LO case, which can be attributed to the smaller amount of air with ambient temperature that enters the building enclosure.

Fig. 12 shows the surface temperatures at the heated wall measured by the infrared camera. Note that these are instantaneous values measured under stationary conditions, as opposed to the time-averaged temperatures reported above. The surface temperatures are also normalized by T_{ref}, i.e., 25.5 °C for both cases. The highest measured dimensionless surface temperature, $(T-T_{ref})/T_{ref}$, is 0.8 for the LO case and 0.82 for the SO case. The surface temperature distribution shows some similarities between both cases, with higher temperatures measured at the height of the openings and at the upper part of the heated wall, just below the ceiling. This can be attributed to the flow field close to these parts of the heated wall, with possibly recirculation areas with very low velocities in these areas and thus reduced convective cooling of this part of the wall by the incoming air. Since the openings are not present along the entire width of the building, low velocity regions are expected close to the side walls. Note that the blue spot at the bottom in both figures is the effect of a temperature sensor taped to the heated wall for the purpose of thermal camera calibration.

3.3. Heat flux

Fig. 13 shows time-averaged values of the surface heat flux measured at six locations on the heated wall (see Fig. 5c and right side of Fig. 13). The surface heat fluxes measured for the LO case are up to 20 % larger (ID1) compared to the SO case. However, near the bottom of the heated wall, close to the windward opening (ID4), the surface heat flux measured for the LO case is 9.6 % smaller than for the SO case. This can – at least partly – be attributed to local differences in the complex transient flow field including the more downward deflection of the incoming yet as shown in Fig. 6c and d, which is expected to drive more intensive recirculation zones near ID4. The highest heat fluxes, i.e. 556.6 W/m^2 and 510.3 W/m^2 for the LO case and the SO case, respectively, are measured near the bottom in the center of the heated wall (ID5). These highest values are expected to be related to flow impingement and reattachment at this location, and to pronounced jet flapping at this location [49]. The lowest heat fluxes, i.e. 317.2 W/m^2 for the LO case and 260.5 W/m^2 for the SO case, are observed at the upper part of the heated wall (ID2) and are expected to be related to low local velocities

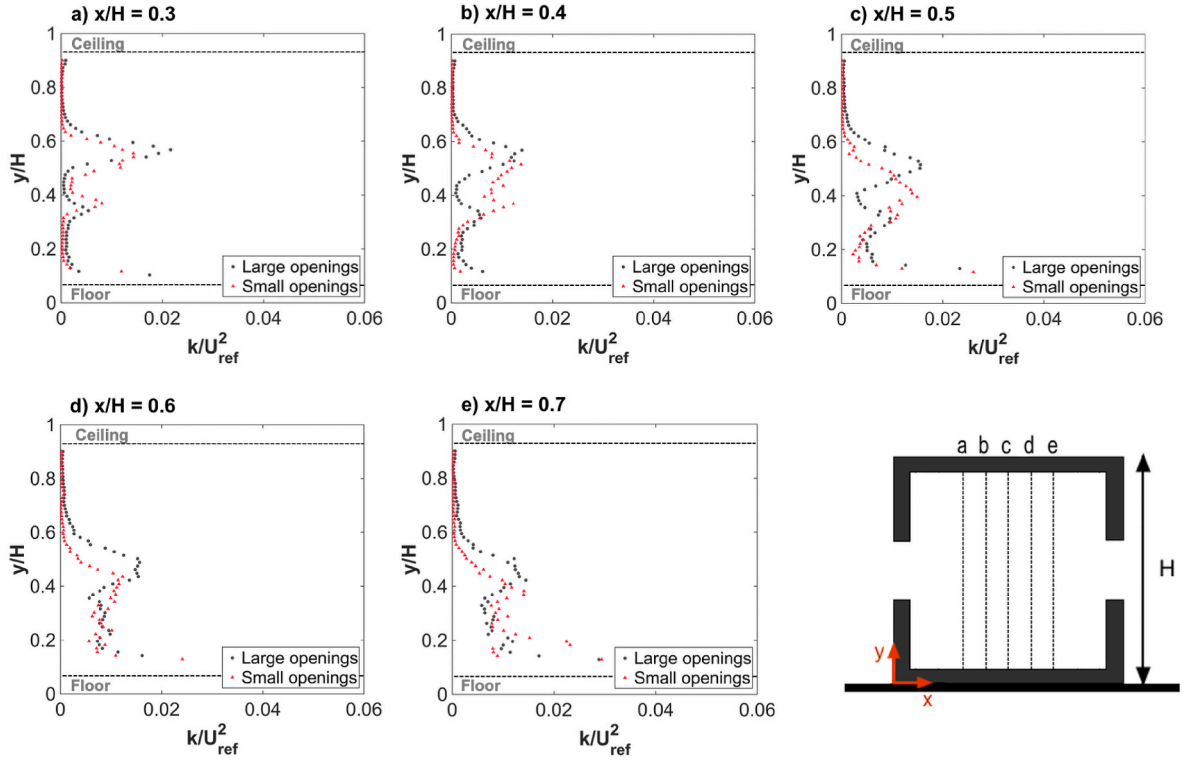

Fig. 10. Dimensionless time-averaged vertical profiles of k/U_{ref}^2 for large and small openings along five lines in the vertical centerplane (z/H = 0.5); U_{ref} = 1.9 m/s.

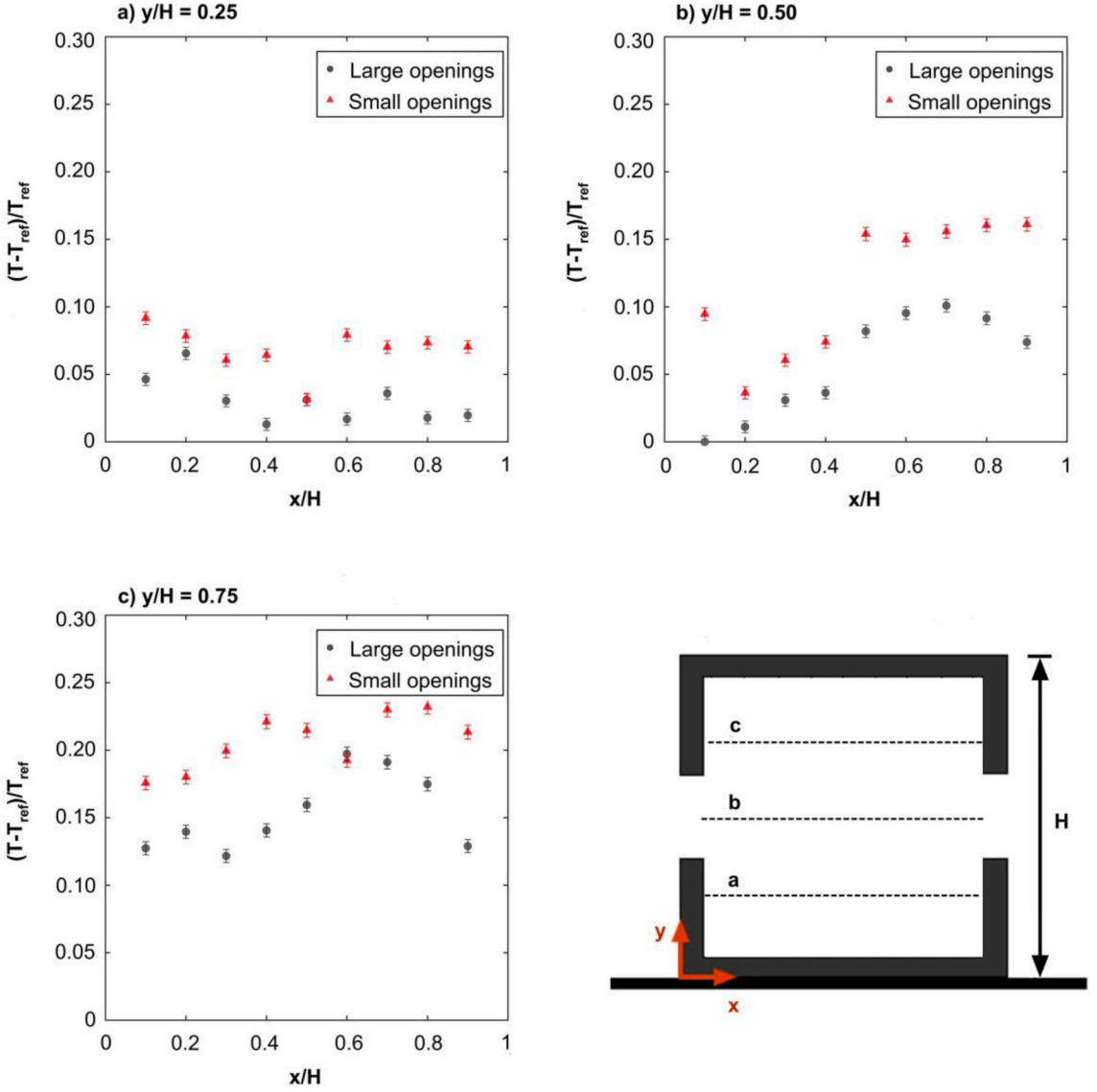

Fig. 11. Relative difference in time-averaged air temperatures, $(T-T_{ref})/T_{ref,}$ measured along three horizontal lines in the vertical centerplane; (a) $y/H = 0.25$, (b) $y/H = 0.5$ and (c) $y/H = 0.75$, $T_{ref} = 25.5$ °C.

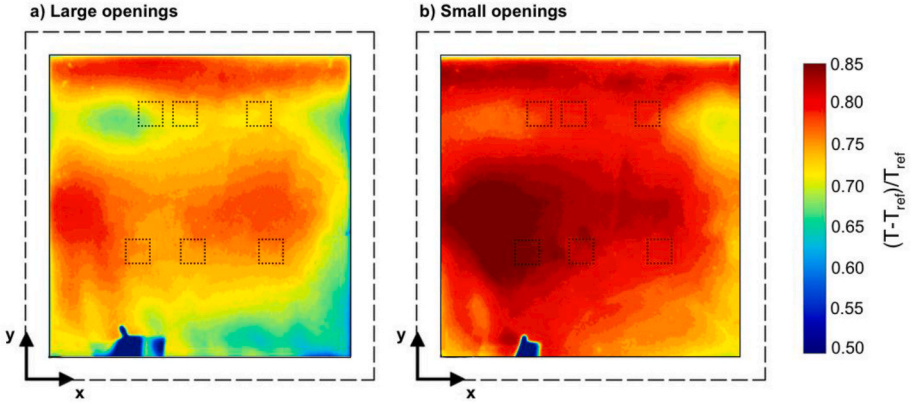

Fig. 12. Dimensionless temperature at the interior surface of the heated wall, $(T-T_{ref})/T_{ref}$. (a) Building model with large openings. (b) Building model with small openings.

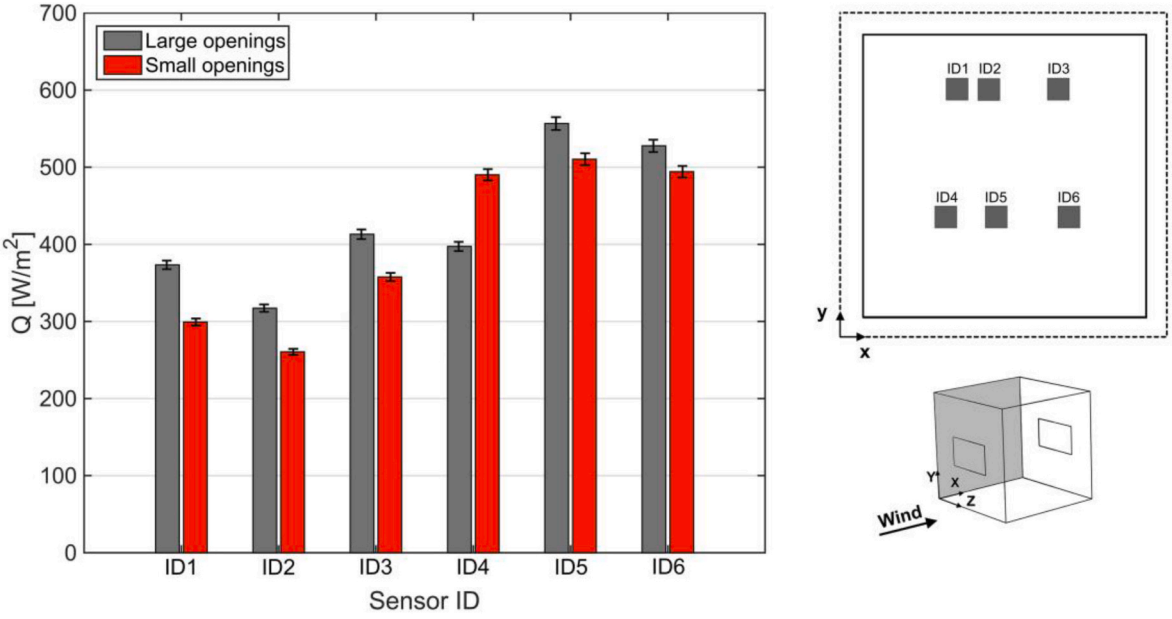

Fig. 13. Surface heat flux (W/m^2) measured at the six different positions at the interior surface of the heated wall.

and flow recirculation. The measured higher surface heat fluxes for the LO case are consistent with the observed higher velocities inside the building and the associated larger amount of cold ambient air entering the building; both will induce higher heat transfer rates from the heated wall.

4. Analysis of convective heat transfer coefficients and correlations

An accurate estimation of the CHTC for interior surfaces (i.e. internal CHTC) is crucial for modeling ventilative cooling and the resulting cooling energy demands in building energy simulations (BES). However, for internal convective heat transfer in buildings with large openings, where the flow can be dominated by wind (inertial) forces rather than buoyancy, it might be difficult to choose the right correlation to obtain accurate values for the CHTC. Many internal CHTC correlations are based on natural convection, whereas the internal CHTCs for forced and mixed convection were mostly developed for mechanical ventilation [54–58]. Both types of correlations might thus not be applicable for natural ventilative cooling cases. This subsection explores the applicability of existing internal CHTC correlations for convective heat transfer in case of natural ventilative cooling.

The CHTC can be defined as

$$h_c = \frac{q}{T_s - T_{air}} \tag{7}$$

where q is the convective heat flux density in W/m^2, T_s is the surface temperature and T_{air} is the ambient (outdoor) temperature. T_{air} is equal to 25.5 °C for both opening sizes.

Several limitations of the existing correlations for the internal CHTC in the framework of ventilative cooling can be noted. Many existing correlations often only use the temperature difference between the surface and the adjacent air, since this is generally the main driving force for indoor convective heat transfer, where the local velocities are generally low and buoyancy plays an important role (natural convection). In the case of internal CHTC correlations for forced convection, the existing correlations are restricted to low velocities and volume flow rates [54].

In order to provide a comparison between the experimentally obtained CHTC by the wind tunnel measurements and the CHTC from the literature, appropriate scaling must be applied for dynamic similarity. Dynamic similarity for forced convection strictly demands equality of three dimensionless numbers in full scale and reduced scale: Re, the Prandtl number (Pr) and the Nusselt number (*Nu*). The full-scale equivalent of the building model is a building with a (floor) height of 3 m. The reference wind speed U_{ref} is kept at 1.9 m/s in both reduced scale and full scale, the temperatures are kept the same, and also the fluid is kept the same, implying the same viscosity and density in reduced scale and full scale. The Ri number is 0.03 and 0.51 in reduced scale and full scale, respectively, denoting the dominance of forced convection, albeit that this is more pronounced at reduced scale. The reduced-scale building Reynolds number is 18,269 which evidently is much smaller than the full-scale value of 365,385, but the reduced-scale value is above the critical value of 11,000 [27] and the building has sharp outer edges, leading to fixed separation points. The Pr number is the same in full scale and reduced scale because the fluid and the temperatures are the same. Therefore, in order to scale the CHTC the Nusselt number should be used:

$$Nu = \frac{hL}{k} \tag{8}$$

where h is the CHTC (W/m^{2}K), L is the length scale (m) – height of the building in this case, and k is the thermal conductivity of air (W/mK). In order to convert the measured reduced-scale *Nu* to full-scale, the experimental CHTC values need to be divided by a scaling factor of 20, which is the ratio between the length scale at full scale and reduced scale. These full-scale CHTCs will be compared with internal CHTC correlations from the literature.

The full-scale internal CHTCs at each of the six surface heat flux measurement locations, calculated using Eq. (7), are compared with the internal CHTC ($h_{c,i}$) values obtained by correlations from the literature (Table 2). The heat fluxes are measured on the vertical heated wall, therefore, only internal CHTC correlations applicable for vertical walls are used for the analysis. The correlation for vertical surfaces provided by TRNSYS [59] is based on the difference between surface temperature and temperature of the ambient air. The correlation from Beausoleil-Morrison ([60 [, [61]) is based on either the ventilation rate and/or the temperature difference for opposing forces (e.g. mechanical and buoyant forces acting in opposite direction). To create an adaptive CHTC correlation, Beausoleil-Morrison used the Churchill and Usagi

Table 2
Internal convective heat transfer coefficient ($h_{c,i}$) correlations obtained from literature.

Source	Correlation	Reference temperature
TRNSYS [59]	$h_c = 1.5(T_s - T_{air})^{0.25}$	T_{air} [a]
Beausoleil-Morrison [60,61]	$h_c = \max\left\{ \begin{array}{c} \left[\left[\left(1.5(\Delta T/H)^{1/4}\right)^6 + \left(1.23\Delta T^{1/3}\right)^6\right]^{3/6} - \left[\left((T_S - T_{sup})/\Delta T\right)\left(-0.199 + 0.19ACH^{0.8}\right)\right]^3\right]^{1/3} \\ 0.8\left\{\left[1.5(\Delta T/H)^{1/4}\right]^6 + \left[1.23\Delta T^{1/3}\right]\right\}^{1/6} \\ 0.8\left[\left((T_s - T_{sup})/\Delta T\right)\left(-0.199 + 0.19ACH^{0.8}\right)\right] \end{array} \right.$	T_{mean} [a]
Khalifa [64]	$h_c = 1.98\lvert\Delta T\rvert^{0.32}$	$T_{room\ average}$
Spitler et al. [57]	$h_c = 1.6 + 92.7J^{0.5}$	–

Notes: T_s - surface temperature, T_{air} – air temperature, H – height of the vertical surface, J – jet momentum number ($(mU_0)/(\rho g V_{room})$) - J outside limits (>0.011), m – mass flow rate, U_0 – supply velocity, ρ – density of surrounding air, g – gravitational acceleration, V_{room} – volume of the room, T_{sup} – air supply temperature, ΔT – surface to air temperature difference.
[a] Room average.

[62] correlation for mixed convection regimes and blended it with the correlation for forced convection by Fisher [54] and with the correlation for natural convection developed by Alamdari and Hammond [63]. The correlation provided by Khalifa [64] is based on experiments for heated surfaces in a test chamber with the average room temperature as reference temperature. Finally, Spitler et al. [57] developed a CHTC correlation based on a range of full-scale experiments in a test chamber for high volume flow rates (i.e. ACH >15 h^{-1}). The authors found that in most of the studied cases, convective heat transfer is linearly proportional to the bulk velocity, which is in turn proportional to the square root of dimensionless jet momentum flux.

For all correlations, the ambient air temperature (T_{air} = 25.5 °C for both opening sizes) is chosen as a reference temperature. The surface temperature (T_s) is chosen as the temperature of the heated wall at a given measurement location (ID1−ID6). The height of the vertical surface (H) in the correlation by Beausoleil-Morrison ([60,61]) corresponds to 2.6 m, which is the full-scale height of the heated wall. The correlation by Spitler et al. [57] uses a velocity of the supply jet to calculate the CHTC (U_0 = 0.067 m/s), this value corresponds to the full-scale jet velocity at y/H = 0.75 and x/H = 0.1.

Fig. 14 shows the comparison between the full-scale internal CHTCs obtained by the above-mentioned CHTC correlations and the values calculated from the measurements. The CHTCs calculated from the experiments are in most cases substantially larger than CHTCs calculated using the correlations from the literature. For the LO case (Fig. 14a), the correlations from literature, except the one from Spitler et al. [57], underpredict the CHTC with up to 79.0 % (($CHTC_{exp}$-$CHTC_{correlation}$)/$CHTC_{exp}$), which may lead to incorrect predictions of the ventilative cooling effect on the energy demand of buildings. The CHTC correlation by Spitler et al. [57] overpredicts the CHTC at all locations with an average overprediction of CHTC by 49 %, with differences that vary between 16 % (ID3) and 101 % (ID2). The correlation by Beausoleil-Morrison [60] underpredicts the CHTC at all locations, (differences between 29.9 % (ID2) to 60 % (ID3)), with an average difference of 52 %, which is better than the CHTC correlations by Kalifa [64] and TRNSYS [59]. Given the large number of governing parameters involved, the agreement between the correlations of Spitler et al. [57] and Beausoleil-Morrison [60] and the experiments is considered fairly good for the LO case.

Fig. 14b shows that in the configuration with small openings, the CHTCs calculated based on correlations from literature, except the one from Spitler et al. [57], are also significantly lower (up to 76.8 %), than those from the experiments. The average CHTC by Spitler et al. [57] is about 69.8 % higher than the average CHTC based on experiments for the SO case. Similarly, as in the LO case, the correlation by Beausoleil-Morisson [60] underpredicts CHTC at all locations with differences varying from 4 % (ID2) to 54 % (ID5). Again, the agreement between the correlation from Beausoleil-Morisson [60] and experiments emerges as fairly good given all parameters involved.

Fig. 14 shows negligible or zero variation across the heated plate for all correlations from the literature. This is in contrast with results obtained by experimental data, where internal CHTCs vary up to 42.1 % for large openings and up to 42.2 % for small openings. This variation is mainly caused by the larger heat fluxes measured at the top of the heated wall (ID1). Internal CHTCs based on the correlations from literature listed in Table 2 show only a small deviation compared to the average CHTC value – up to 2 % for both large and small openings. CHTCs based on the measured heat fluxes show higher deviations from the average CHTC; up to 26 % lower (ID2) to 28 % higher (ID3) for large openings (Fig. 14a) and up to 37 % (ID1) lower and 30 % (ID5) higher for small

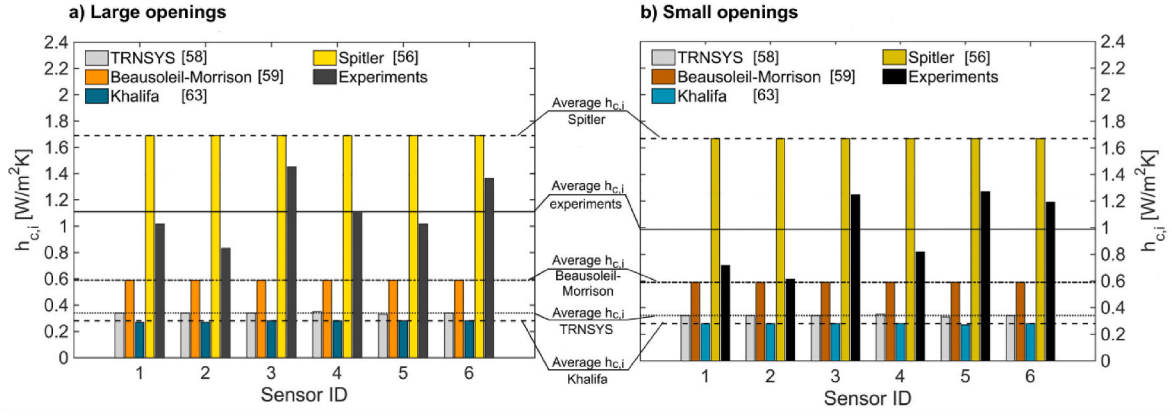

Fig. 14. Internal convective heat transfer coefficient $h_{c,i}$ (W/m^{2}K) based on internal convective heat transfer correlations and the measurements at the six positions at the interior surface of the heated wall.

openings (Fig. 14b). These larger deviations from the average CHTC value can be attributed to the fact that the surface temperatures and heat fluxes vary considerably over the heated plate. Because CHTC correlations generally try to capture a large physical complexity into relatively simple expressions, it would indeed be disproportionate to expect them to be able to accurately take into account specific differences in terms of position on the wall.

Fig. 14 shows that the influence of the opening size on the internal CHTC is not reproduced by the correlations from the literature, because these correlations mainly take into account the temperature difference between the surface temperature and the temperature of the ambient air and do not take into account the heat flux, which is largely influenced by the temperature and the flow field inside the enclosure in general and the flow near the wall in particular.

5. Discussion

The main objective of this study is to provide an analysis of indoor air velocities, temperatures and heat fluxes in a non-isothermal cross ventilation flow.

To the best knowledge of the authors, this is the first study to provide insights into a combination of indoor airflow, indoor air temperature distribution and surface heat flux distribution in a building with a heated wall.

This study has the following limitations:

- Velocities were obtained only in the vertical centerplane, future research will also focus on other planes inside similar enclosures.
- Buoyancy only has a small effect on the indoor airflow pattern. Future work will focus on scenarios where buoyancy has a larger effect on the indoor airflow (higher Richardson numbers).
- Experiments were performed for one wind direction. However, it would be interesting to investigate the influence of different wind directions on non-isothermal cross-ventilative cooling.
- Only two opening sizes and one location have been studied. Future work could focus on other opening sizes and locations to extend the impact of the results obtained.
- Only one of the sidewalls of the building model was heated. Future work will include experiments where other surfaces of the building model can be heated.
- Due to the size restrictions of the wind-tunnel cross-section it was only possible to achieve $Gr = 10^7$, implying laminar convection close to the heated wall. The type of flow close to the heated wall has an influence on convective heat transfer, therefore, care is needed when trying to reproduce this case using CFD simulations as the correct modeling of the wall – fluid interaction especially in non-isothermal cases is crucial for the accuracy of the results.
- The large window opening dimensions and approach flow conditions used in this study ($U_{ref} = 1.9$ m/s and no upstream obstacles) yield a full-scale air exchange rate (ACH) of about 218 h^{-1}. Future studies could assess the flow field, and moreover, the CHTC values and correlations, for other ACH values.
- The focus was on cross ventilation via openings in the windward and leeward facade. Future studies could focus on detailed non-isothermal experiments for natural ventilation configurations with supply or exhaust via openings in the roof of the building, as for example studied by Refs. [65–67].
- The link to thermal comfort and indoor air quality is not made in this paper. Future work could connect the detailed results from this generic study in terms of velocity, temperature, etc., to applications, such as thermal comfort and pollutant dispersion.

6. Conclusions

This paper presented measurements of velocities, air temperatures, surface temperatures and surface heat flux in a reduced-scale cross-ventilated generic building with one heated wall. The measurements are performed both for large openings (LO case) and small openings (SO case). In addition, this paper presents a comparison of the up-scaled experimentally derived internal CHTCs with CHTCs based on correlations from literature. The main objectives of this study are: the analysis of indoor velocities, temperatures, heat fluxes and CHTCs, a comparison between experimentally derived CHTCs with CHTCs based on correlations from literature, and the collection of an experimental data set for the validation of CFD studies of non-isothermal cross-ventilative cooling. The following main conclusions can be drawn from this study:

- The flow through the building is dominated by a jet flow from the windward to the leeward opening. In both cases – LO case and SO case – the jet deflects downwards immediately after passing through the windward opening.
- Time-averaged streamwise velocities measured in the vertical centerplane along the lines close to the windward opening are similar for the LO case and the SO case, however, from the central region towards the leeward opening of the building ($0.4 < x/H < 1$) larger velocities are observed in the LO case. Moreover, the location of maximum velocity in the LO case differs from the SO case, which is due to the more significant loss of momentum of the jet after passing through the windward opening in the SO case.
- Higher indoor air temperatures are measured along the horizontal line close to the leeward opening and along the upper horizontal line for both cases. The highest dimensionless air temperatures, i.e. $(T-T_{ref})/T_{ref}$, are measured along the upper horizontal line for both cases; i.e. 0.20 for LO case and 0.23 for SO case, which is 20 % and 23 % higher than the reference temperatures, respectively.
- Overall, air temperatures in the SO case are up to 7.5 % higher compared to the LO case. This can be attributed to the lower velocities and lower volume flow rate for the building with the small openings, which results in a smaller cooling effect of the jet.
- Overall, the surface heat fluxes measured on the heated wall for the LO case are 9–20 % larger than those in the SO case, which can be attributed to the larger amount of cold air entering the building and the higher velocities inside the building for the LO case, resulting in an increased convective heat transfer from the heated wall to the indoor air of the building model. The internal CHTC ($h_{c,i}$) based on the measured heat fluxes varies considerably across the heated wall – up to 28 % and 37 % for LO and SO, respectively. This is attributed to the variation of temperature and heat flux across the heated wall. However, this is not the case for internal CHTC obtained using correlations from literature, where its variation across the heated wall is significantly lower; i.e. only up to 2 % for the LO case.
- The impact of the opening size on the values of CHTC calculated using correlations for internal convective heat transfer from literature is negligible However, for the CHTCs based on the measured heat flux, the influence of the opening size is more significant, as the average CHTC is up to 15 % higher for the LO case than for the SO case. These differences can be attributed to the amount of cold air entering the building through openings and its effect on the heat transfer from the wall.
- The values of internal CHTC based on the measured heat fluxes are up to 5 times higher (ID5) than internal CHTC based on correlations from literature.
- In most cases, the literature based correlations for internal CHTC significantly underestimate CHTC. Indeed, existing correlations for internal convection were not developed for naturally ventilated buildings with large openings and are therefore not suitable for ventilative cooling. However, the correlation by Beausoleil-Morrison [60] shows a fairly good agreement with the experimentally obtained CHTC for the SO case (40 % difference compared to average CHTC from experiments), however, locally, differences still vary considerably (from 4 % to 54 %). Furthermore, for the LO case, a fairly good agreement with experimentally obtained CHTC is again

shown for the correlation by Beausoleil-Morrison [60] (difference of 52 % from the average experimentally derived CHTC), and for the correlation by Spitler [57] (49 % difference compared to averaged CHTC from experiments).

Because CHTC correlations generally try to capture a large physical complexity into relatively simple expressions, it would be indeed disproportionate to expect them to be able to accurately take into account specific differences in terms of position on the wall from the inlet opening.

CRediT authorship contribution statement

Katarina Kosutova: Writing – original draft, Project administration, Methodology, Formal analysis, Data curation, Conceptualization. **Christina Vanderwel:** Writing – review & editing, Supervision. **Twan van Hooff:** Writing – review & editing, Supervision. **Bert Blocken:** Writing – review & editing, Supervision. **Jan L.M. Hensen:** Writing – review & editing, Supervision.

Declaration of competing interest

The authors declare that they have no known competing financial interests or personal relationships that could have appeared to influence the work reported in this paper.

Data availability

Data will be made available on request.

Acknowledgements

The authors are thankful to Geert-Jan Maas and Jan Diepens from Eindhoven University of Technology for their help in the construction and development of the experimental building model and to Neil Gillam from the University of Southampton for his help and support during the wind-tunnel experiments.

References

[1] D. Etheridge, Natural Ventilation of Buildings: Theory, Measurement and Design, John Wiley & Sons Ltd., United Kingdom, 2012.
[2] H.B. Awbi, Ventilation of Buildings, Spon Press, London, New York, 2003.
[3] Q. Chen, Ventilation performance prediction for buildings: a method overview and recent applications, Build. Environ. 44 (4) (Apr. 2009) 848–858, https://doi.org/10.1016/j.buildenv.2008.05.025.
[4] P. Karava, T. Stathopoulos, A.K. Athienitis, Airflow assessment in cross-ventilated buildings with operable façade elements, Build. Environ. 46 (1) (2011) 266–279, https://doi.org/10.1016/j.buildenv.2010.07.022.
[5] G. Carrilho da Graça, P. Linden, Ten questions about natural ventilation of non-domestic buildings, Build. Environ. 107 (Oct. 2016) 263–273, https://doi.org/10.1016/j.buildenv.2016.08.007.
[6] S.M. Dutton, D. Banks, S.L. Brunswick, W.J. Fisk, Health and economic implications of natural ventilation in California offices, Build. Environ. 67 (Sep. 2013) 34–45, https://doi.org/10.1016/j.buildenv.2013.05.002.
[7] Z. Tong, Y. Chen, A. Malkawi, Z. Liu, R.B. Freeman, Energy saving potential of natural ventilation in China: the impact of ambient air pollution, Appl. Energy 179 (Oct. 2016) 660–668, https://doi.org/10.1016/j.apenergy.2016.07.019.
[8] T. van Hooff, B. Blocken, Coupled urban wind flow and indoor natural ventilation modelling on a high-resolution grid: a case study for the Amsterdam ArenA stadium, Environ. Model. Software 25 (1) (Jan. 2010) 51–65, https://doi.org/10.1016/j.envsoft.2009.07.008.
[9] N. Artmann, H. Manz, P. Heiselberg, Climatic potential for passive cooling of buildings by night-time ventilation in Europe, Appl. Energy 84 (2) (Feb. 2007) 187–201, https://doi.org/10.1016/j.apenergy.2006.05.004.
[10] V. Geros, M. Santamouris, S. Karatasou, A. Tsangrassoulis, N. Papanikolaou, On the cooling potential of night ventilation techniques in the urban environment, Energy Build. 37 (3) (Mar. 2005) 243–257, https://doi.org/10.1016/j.enbuild.2004.06.024.
[11] M. Santamouris, A. Sfakianaki, K. Pavlou, On the efficiency of night ventilation techniques applied to residential buildings, Energy Build. 42 (8) (Aug. 2010) 1309–1313, https://doi.org/10.1016/j.enbuild.2010.02.024.
[12] L.-X. Wu, J.-N. Zhao, Z.-J. Wang, Night ventilation and active cooling coupled operation for large supermarkets in cold climates, Energy Build. 38 (12) (Dec. 2006) 1409–1416, https://doi.org/10.1016/j.enbuild.2006.02.011.
[13] G. Carrilho da Graça, Q. Chen, L.R. Glicksman, L.K. Norford, Simulation of wind-driven ventilative cooling systems for an apartment building in Beijing and Shanghai, Energy Build. 34 (1) (Jan. 2002) 1–11, https://doi.org/10.1016/S0378-7788(01)00083-4.
[14] R. Ramponi, A. Angelotti, B. Blocken, Energy saving potential of night ventilation: sensitivity to pressure coefficients for different European climates, Appl. Energy 123 (Jun. 2014) 185–195, https://doi.org/10.1016/j.apenergy.2014.02.041.
[15] K. Goethals, H. Breesch, A. Janssens, Sensitivity analysis of predicted night cooling performance to internal convective heat transfer modelling, Energy Build. 43 (9) (Sep. 2011) 2429–2441, https://doi.org/10.1016/j.enbuild.2011.05.033.
[16] S. Leenknegt, R. Wagemakers, W. Bosschaerts, D. Saelens, Numerical study of convection during night cooling and the implications for convection modeling in Building Energy Simulation models, Energy Build. 64 (Sep. 2013) 41–52, https://doi.org/10.1016/j.enbuild.2013.04.012.
[17] J. Le Dréau, P. Heiselberg, R.L. Jensen, Experimental investigation of convective heat transfer during night cooling with different ventilation systems and surface emissivities, Energy Build. 61 (Jun. 2013) 308–317, https://doi.org/10.1016/j.enbuild.2013.02.021.
[18] J. Pfafferott, S. Herkel, M. Jäschke, Design of passive cooling by night ventilation: evaluation of a parametric model and building simulation with measurements, Energy Build. 35 (11) (Dec. 2003) 1129–1143, https://doi.org/10.1016/j.enbuild.2003.09.005.
[19] N. Artmann, R.L. Jensen, H. Manz, P. Heiselberg, Experimental investigation of heat transfer during night-time ventilation, Energy Build. 42 (3) (Mar. 2010) 366–374, https://doi.org/10.1016/j.enbuild.2009.10.003.
[20] P. Blondeau, M. Spérandio, F. Allard, Night ventilation for building cooling in summer, Sol. Energy 61 (5) (Nov. 1997) 327–335, https://doi.org/10.1016/S0038-092X(97)00076-5.
[21] V. Geros, M. Santamouris, A. Tsangrasoulis, G. Guarracino, Experimental evaluation of night ventilation phenomena, Energy Build. 29 (2) (Jan. 1999) 141–154, https://doi.org/10.1016/S0378-7788(98)00056-5.
[22] T. Kubota, D.T.H. Chyee, S. Ahmad, The effects of night ventilation technique on indoor thermal environment for residential buildings in hot-humid climate of Malaysia, Energy Build. 41 (8) (Aug. 2009) 829–839, https://doi.org/10.1016/j.enbuild.2009.03.008.
[23] B. Blocken, LES over RANS in building simulation for outdoor and indoor applications: a foregone conclusion? Build. Simulat. 11 (5) (2018) 821–870, https://doi.org/10.1007/s12273-018-0459-3.
[24] B. Blocken, 50 years of computational wind engineering: past, present and future, J. Wind Eng. Ind. Aerod. 129 (Jun. 2014) 69–102, https://doi.org/10.1016/j.jweia.2014.03.008.
[25] B. Blocken, Computational Fluid Dynamics for urban physics: importance, scales, possibilities, limitations and ten tips and tricks towards accurate and reliable simulations, Build. Environ. 91 (Sep. 2015) 219–245, https://doi.org/10.1016/j.buildenv.2015.02.015.
[26] S. Leenknegt, R. Wagemakers, W. Bosschaerts, D. Saelens, Numerical sensitivity study of transient surface convection during night cooling, Energy Build. 53 (Oct. 2012) 85–95, https://doi.org/10.1016/j.enbuild.2012.06.020.
[27] W.H. Snyder, I.P. Castro, The critical Reynolds number for rough-wall boundary layers, J. Wind Eng. Ind. Aerod. 90 (1) (2002) 41–54, https://doi.org/10.1016/S0167-6105(01)00114-3.
[28] B. Ruck, Wind-tunnel measurements of flow field characteristics around a heated model building, J. Wind Eng. Ind. Aerod. 50 (Dec. 1993) 139–151, https://doi.org/10.1016/0167-6105(93)90069-Z.
[29] A. Bejan, J.L. Lage, The Prandtl number effect on the transition in natural convection along a vertical surface, J. Heat Tran. 112 (3) (1990) 787–790.
[30] K. Richards, M. Schatzmann, B. Leitl, Wind tunnel experiments modelling the thermal effects within the vicinity of a single block building with leeward wall heating, J. Wind Eng. Ind. Aerod. 94 (8) (Aug. 2006) 621–636, https://doi.org/10.1016/j.jweia.2006.02.003.
[31] Y. Tominaga, B. Blocken, Wind tunnel experiments on cross-ventilation flow of a generic building with contaminant dispersion in unsheltered and sheltered conditions, Build. Environ. 92 (2015) 452–461, https://doi.org/10.1016/j.buildenv.2015.05.026.
[32] Y. Tominaga, B. Blocken, Wind tunnel analysis of flow and dispersion in cross-ventilated isolated buildings: impact of opening positions, J. Wind Eng. Ind. Aerod. 155 (Aug. 2016) 74–88, https://doi.org/10.1016/j.jweia.2016.05.007.
[33] P.S. Carey, D.W. Etheridge, Direct wind tunnel modelling of natural ventilation for design purposes, Build. Serv. Eng. Res. Tecnol. 20 (3) (Aug. 1999) 131–142, https://doi.org/10.1177/014362449902000305.
[34] S. Murakami, S. Kato, S. Akabayashi, Y. Tominaga, Wind tunnel test on velocity-pressure field of cross-ventilation with open windows, Build. Eng. 97 (1991) 525–538.
[35] T. Katayama, J. Tsutsumi, A. Ishii, Full-scale measurements and wind tunnel tests on cross-ventilation, Spec. Issue 8th Int. Conf. Wind Eng. 1991 44 (1) (Oct. 1992) 2553–2562, https://doi.org/10.1016/0167-6105(92)90047-E.
[36] S. Kato, S. Murakami, A. Mochida, S. Akabayashi, Y. Tominaga, Velocity-pressure field of cross ventilation with open windows analyzed by wind tunnel and numerical simulation, Spec. Issue 8th Int. Conf. Wind Eng. 44 (1) (1991) 2575–2586, https://doi.org/10.1016/0167-6105(92)90049-G. Oct. 1992.
[37] M. Ohba, K. Irie, T. Kurabuchi, Study on airflow characteristics inside and outside a cross-ventilation model, and ventilation flow rates using wind tunnel experiments,

J. Wind Eng. Ind. Aerod. 89 (14) (Dec. 2001) 1513–1524, https://doi.org/10.1016/S0167-6105(01)00130-1.
[38] Y. Jiang, D. Alexander, H. Jenkins, R. Arthur, Q. Chen, Natural ventilation in buildings: measurement in a wind tunnel and numerical simulation with large-eddy simulation, J. Wind Eng. Ind. Aerod. 91 (3) (Feb. 2003) 331–353, https://doi.org/10.1016/S0167-6105(02)00380-X.
[39] P. Karava, T. Stathopoulos, A.K. Athienitis, Wind-induced natural ventilation analysis, Sol. Energy 81 (1) (Jan. 2007) 20–30, https://doi.org/10.1016/j.solener.2006.06.013.
[40] L. Ji, H. Tan, S. Kato, Z. Bu, T. Takahashi, Wind tunnel investigation on influence of fluctuating wind direction on cross natural ventilation, Build. Environ. 46 (12) (Dec. 2011) 2490–2499, https://doi.org/10.1016/j.buildenv.2011.06.006.
[41] L. James Lo, D. Banks, A. Novoselac, Combined wind tunnel and CFD analysis for indoor airflow prediction of wind-driven cross ventilation, Build. Environ. 60 (Feb. 2013) 12–23, https://doi.org/10.1016/j.buildenv.2012.10.022.
[42] A. Tecle, G.T. Bitsuamlak, T.E. Jiru, Wind-driven natural ventilation in a low-rise building: a Boundary Layer Wind Tunnel study, Build. Environ. 59 (Jan. 2013) 275–289, https://doi.org/10.1016/j.buildenv.2012.08.026.
[43] S. Taddei, C. Manes, B. Ganapathisubramani, Characterisation of drag and wake properties of canopy patches immersed in turbulent boundary layers, J. Fluid Mech. 798 (Jul. 2016) 27–49, https://doi.org/10.1017/jfm.2016.312.
[44] C. Vanderwel, B. Ganapathisubramani, Effects of spanwise spacing on large-scale secondary flows in rough-wall turbulent boundary layers, J. Fluid Mech. 774 (2015) R2, https://doi.org/10.1017/jfm.2015.292.
[45] B. Blocken, T. Stathopoulos, J. Carmeliet, Wind environmental conditions in passages between two long narrow perpendicular buildings, J. Aero. Eng. 21 (4) (Oct. 2008) 280–287, https://doi.org/10.1061/(ASCE)0893-1321(2008)21:4(280).
[46] N.J. Cook, Determination of the model scale factor in wind-tunnel simulations of the adiabatic atmospheric boundary layer, J. Wind Eng. Ind. Aerod. 2 (4) (1978) 311–321, https://doi.org/10.1016/0167-6105(78)90016-8.
[47] J.B. Barlow, W.H. Rae Jr., Low-speed Wind Tunnel Testing, John Wiley & Sons Ltd., New York, 1999.
[48] W.H. Snyder, Guideline for Fluid Modeling of Atmospheric Diffusion, US Environmental Protection Agency, S, Apr. 1981. Report EPA-600/8-81-009, https://ui.adsabs.harvard.edu/abs/1981gfma.book.
[49] A.K. Prasad, Particle image velocimetry, Curr. Sci. 79 (2000) 51–60.
[50] H.W. Coleman, W.G. Steel, Experimentation and Uncertainty Analysis for Engineers, Wiley, New York, 1999.
[51] T. van Hooff, B. Blocken, T. Defraeye, J. Carmeliet, G.J.F. van Heijst, PIV measurements of a plane wall jet in a confined space at transitional slot Reynolds numbers, Exp. Fluid 53 (2) (Aug. 2012) 499–517, https://doi.org/10.1007/s00348-012-1305-5.
[52] T. van Hooff, B. Blocken, Y. Tominaga, On the accuracy of CFD simulations of cross-ventilation flows for a generic isolated building: comparison of RANS, LES and experiments, Build. Environ. 114 (Mar. 2017) 148–165, https://doi.org/10.1016/j.buildenv.2016.12.019.
[53] T. Kurabuchi, A. Arashiguchi, T. Iwabuchi, Numerical study of airflow structure of a cross-vdentilated model building, in: Ir Distribution in Rooms: Ventilation for Health and Sustainable Environment, 2000, pp. 313–318. Amsterdam.
[54] D. Fisher, C. Pederson, Convective heat transfer in building energy and thermal load calculations, Build. Eng. 103 (1997) 137–148.
[55] A. Novoselac, B.J. Burley, J. Srebric, Development of new and validation of existing convection correlations for rooms with displacement ventilation systems, Energy Build. 38 (3) (Mar. 2006) 163–173, https://doi.org/10.1016/j.enbuild.2005.04.005.
[56] K. Goldstein, A. Novoselac, Convective heat transfer in rooms with ceiling slot diffusers (RP-1416), HVAC R Res. 16 (5) (Sep. 2010) 629–655, https://doi.org/10.1080/10789669.2010.10390925.
[57] J.D. Spitler, C.O. Pedersen, D.E. Fisher, Interior convective heat transfer in buildings with large ventilative flow rates, Build. Eng. 97 (pt 1) (1991) 505–515.
[58] H.B. Awbi, A. Hatton, Mixed convection from heated room surfaces, Energy Build. 32 (2) (Jul. 2000) 153–166, https://doi.org/10.1016/S0098-8472(99)00063-5.
[59] S.A. Klein, et al., TRNSYS 17: Volume 4, Mathematical Reference, 2010.
[60] I. Beausoleil-Morrison, The Adaptive Coupling of Heat and Air Flow Modelling within Dynamic Whole-Building Simulation, University of Strathclyde, Glasgow, UK, 2000.
[61] I. Beausoleil-Morrison, An algorithm for calculating convection coefficients for internal building surfaces for the case of mixed flow in rooms, Spec. Issue Build. SIMULATION99 33 (4) (Apr. 2001) 351–361, https://doi.org/10.1016/S0378-7788(00)00117-1.
[62] S.W. Churchill, R. Usagi, A general expression for the correlation of rates of transfer and other phenomena, AIChE J. 18 (6) (Nov. 1972) 1121–1128, https://doi.org/10.1002/aic.690180606.
[63] F. Alamdari, G.P. Hammond, Improved data correlations for buoyancy-driven convection in rooms, Build. Serv. Eng. Res. Tecnol. 4 (3) (Aug. 1983) 106–112, https://doi.org/10.1177/014362448300400304.
[64] A.J.N. Khalifa, Heat Transfer Processes in Buildings, University of Wales, 1989.
[65] M.V. Cruz-Salas, J.A. Castillo, G. Huelsz, Effect of windexchanger duct cross-section area and geometry on the room airflow distribution, J. Wind Eng. Ind. Aerod. 179 (2018) 514–523.
[66] M. Alsailani, H. Montazeri, A. Rezaeiha, Towards optimal aerodynamic design of wind catchers: impact of geometrical characteristics, Renew. Energy 168 (2021) 1344–1363, https://doi.org/10.1016/j.renene.2020.12.053.
[67] A. Zaki, R. Sharma, The effect of external airflows on ventilation with a rooftop windcatcher, J. Wind Eng. Ind. Aerod. 219 (2021) 104799, https://doi.org/10.1016/j.jweia.2021.104799.